Baldo Sahlmüller

Production of η Mesons in $\sqrt{s_{NN}} = 200$ GeV d+Au and p+p Collisions Measured by the PHENIX Experiment

— 2004 —

Experimentelle Physik

Production of η Mesons in $\sqrt{s_{NN}} = 200$ GeV d+Au and p+p Collisions Measured by the PHENIX Experiment

Diplomarbeit

von

Baldo Sahlmüller

Universität Münster

Institut für Kernphysik

— August 2004 —

Contents

1 Introduction

> The latest results from the Relativistic Heavy Ion Collider (RHIC), the world's most powerful facility for nuclear physics research, strengthen scientists' confidence that RHIC collisions of gold ions have created unusual conditions and that they are on the right path to discover a form of matter called the quark-gluon plasma, believed to have existed in the first microseconds after the birth of the universe.[BNL03]

These are the first words of a press release from June 2003. At that time, recent results from the different experiments at the Relativistic Heavy Ion Collider lead to strong evidence for a new state of matter created in collisions of gold nuclei at very high energies.

Heavy ion physics examines the behavior of nuclear matter at extreme conditions as very high temperatures, energy densities and pressures. Therefore nuclei of heavy elements as gold or lead are accelerated and collided at very high energies. In such collisions a state of matter may possibly be created in which quarks and gluons are the relevant degrees of freedom. Such a state of matter is called quark-gluon plasma. Standard models explaining the evolution of our universe predict the existence of this state a few microseconds after the big bang.

The RHIC facility started colliding gold nuclei in the year 2000, it reaches collision energies up to 200 GeV per nucleon-nucleon pair for heavy nuclei. Four experiments at the collider examine different properties of the nuclear matter created in such collisions. These measurements are expected to provide a better understanding of the theory of quantumchromodynamics.

The PHENIX[1] experiment has measured the production of different particles in collisions of two gold ions, in collisions of two protons and in collisions of a gold ion with a deuterium ion. The comparison of the particle production in the different reaction systems lead to the assumption that an unusual state of matter has been created in central collisions of gold ions.

As a different behavior in the production of e.g. neutral pions and protons has been observed, studies on the production of the η meson can possibly provide further

[1] Pioneering High Energy Nuclear Interaction eXperiment

information on how the particle production in collisions at RHIC energies depends on the particle species. The knowledge of the η production is also important for studies of the production of direct photons in ultrarelativistic collisions.
The outline of this thesis is as follows. First, some basics of nuclear matter at high energies and of ultrarelativistic collisions are given in chapter 2. The PHENIX experiment then is described in chapter 3. The following chapter 4 deals with the different analysis steps which lead to the different results. These results are presented in chapter 5. The behavior of the η meson at high transverse momenta and a comparison with neutral pions are shown as well.

2 Theoretical Basics

2.1 Quarks and Gluons

The structure of matter and the fundamental interaction forces can be described very well by the *standard model*. This theory is based on three kinds of particles: *quarks*, *leptons* and *gauge bosons*. There are six different quarks (down, up, strange, charm, bottom and top) and antiquarks, six different leptons (electron, electron neutrino, muon, muon neutrino, tau and tau neutrino) and antileptons and four types of gauge bosons as the force-carrying particles (gluon, photon, W/Z-boson, graviton). Each of the bosons has an integer spin and mediates one fundamental interaction force. The graviton mediates gravitation, the W- and Z-boson carry the weak interaction, the photon the electromagnetic force and the gluon is the force-carrying particle of the strong force.
Both quarks and leptons are fermions with a spin of $\hbar/2$ and can be divided into three families with two particles each (see Table 2.1). Fermions follow the Fermi-Dirac statistics. According to the Pauli principle, the fermions in a two particle system have to differ in at least one quantum number. In contrast to leptons, quarks are subject to the strong force. Quarks and leptons do not seem to have an internal structure, they seem to be point-like particles. The standard model predicts that matter is entirely composed of quarks and leptons. Each family contains one quark

Fermions	Family			electric	color
	1	2	3	charge	charge
Quarks	u	c	t	+2/3	r, b, g
	d	s	b	-1/3	
Leptons	ν_e	ν_μ	ν_τ	0	–
	e^-	μ^-	τ^-	-1	–

Table 2.1: Quark and lepton families.

with an electric charge of $-2/3$ and one with an electric charge of $+1/3$ in units of the proton charge, the mass of the quarks differs strongly between the three fami-

lies. Analogous to the electric charge in the quantumelectrodynamics (QED), quarks carry the so-called *color charge*. There are three different types of this charge instead of two types of electrical charge. The strong force combines quarks to particles with an integer electrical charge and without color charge, the hadrons. Mesons - hadrons with an integer spin - are composed of a quark and an antiquark which carry color and anticolor; baryons - hadrons with a half-numbered spin - are composed of three quarks, each with a different color charge. Quarks cannot be found as free particles. This observation is called *quark confinement*.
The confinement is based on an important characteristic of the quantumchromodynamics (QCD), the dependence of the strength of the strong force on the distance. The strong force gets weak at small distances between the interacting quarks. When trying to separate two quarks, energy is stored in the color field between them. Due to the strong interaction between the gluons this field is formed like a string. If the distance between the quarks becomes too large, the string breaks and a new quark-antiquark pair and two new strings are generated. It is not possible to get free quarks, instead, new hadrons are produced.
The decreasing strength of the interaction at shorting distances between quarks is predicted by QCD, this property of the theory is the so-called asymptotic freedom. The asymptotic freedom can be seen from the coupling constant of the strong interaction that can be estimated by:

$$\alpha_s = \frac{12\pi}{(33 - 2N_f) \cdot \ln q^2/\Lambda^2} \text{ [Per90].}$$

N_f is the number of the different types of quarks, Λ is the free scaling parameter of QCD while q^2 denotes the four momentum transfer. Λ has to be determined experimentally. Thus α_s is not a real constant, it depends on q^2.

2.2 The Phase Diagram

It is not possible to perform perturbation theory calculations for small momentum transfers, instead one has to work with a discrete space-time lattice. These theoretical calculations predict a phase transition from hadronic matter to quark matter at a certain temperature. At the transition temperature the energy density shows a sharp increase. The temperature at which the transition occurs is the so called

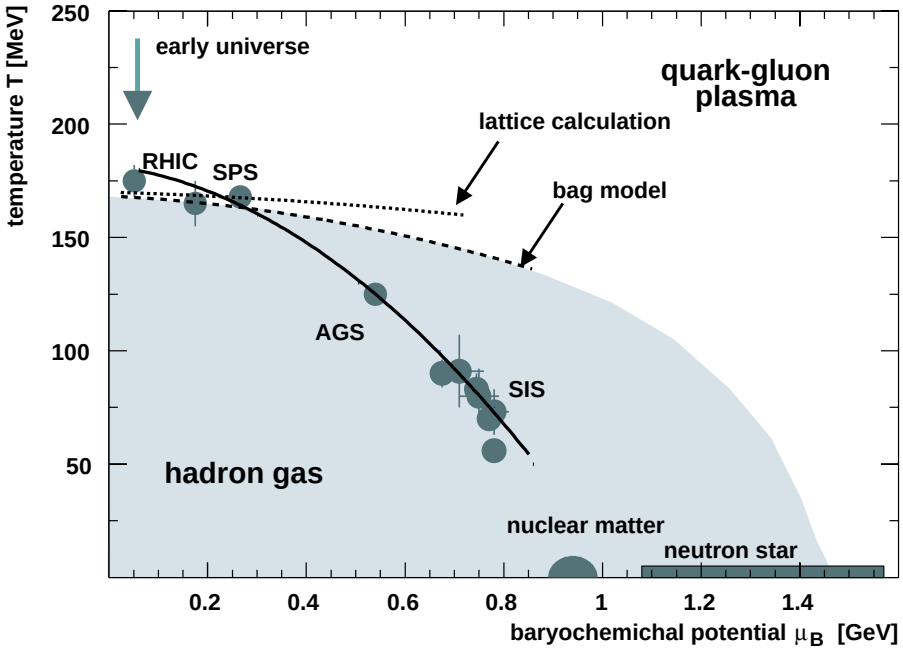

Figure 2.1: Phase diagram of nuclear matter. The phase boundary between a hadronic gas and the QGP is shown as a function of temperature and baryochemical potential μ_B. (according to [Bra01, Cle98])

critical temperature T_C. After the phase transition the quarks and gluons that are normally bound in hadrons can move quasi-freely in a larger region of space. The expected state of matter beyond the phase transition is the quark-gluon plasma (QGP), the process leading to the quasi-free quarks is called *deconfinement*. Phenomenological models furthermore predict a transition to the QGP at high nuclear density in low temperatures.

The phase diagram of hadronic matter as a function of temperature and baryochemical potential μ_B is shown in Figure 2.1. μ_B is a measure of the baryon density of a system, it represents the energy that is necessary to add another baryon to the system. The result of a lattice calculation for $\mu_B = 0$ is given as phase boundary, the critical temperature resulting from the calculation is $T_C \approx 170$MeV. For finite values of μ_B it is difficult to perform lattice calculations, thus the critical temperature has to be extrapolated for $\mu_B > 0$. Therefore a simple, phenomenological bag model has to be used.

In Figure 2.1 two examples of possible phase transitions are shown. The early universe was filled with a quark gluon plasma of high temperature and low baryochemical potential a few milliseconds after the big bang before freezing out to hadronic matter. Today, a QGP at very low temperatures and high μ_B is expected to exist inside neutron stars.
Another transition predicted by QCD calculations is the restoration of chiral symmetry at high temperature and density.

2.3 Ultrarelativistic Collisions

Collisions of atomic nuclei at high energies are performed to create energy densities high enough for the possible production of a quark-gluon plasma. Reactions are called ultrarelativistic if the incoming ions have energies above 10 AGeV. The study of these reactions shall provide information about the strong interaction force, about the equation of state of this hot and dense matter and about possible processes in the early universe.

In heavy ion collisions one distinguishes between the participants, nucleons in the overlap region of the colliding nuclei, and the spectators, the other nucleons. The participants will merge in the so-called fireball, at lower energies they will be completely stopped while they can permeate the arising fireball at higher energies leaving behind a possible QGP with a very small baryon density. The permeation of the participants is called transparency. The spectators do not participate in the reaction and keep their momenta, thus the stroke parameter can be determined by measuring the energy of the spectators along the beam line.
In the beginning of a heavy ion reaction, hard scattering of the quarks occurs and multiple collisions of partons will lead to a high energy density. The system reaches its thermodynamic equilibrium during these scattering processes. Beyond a certain energy density, partonic degrees of freedom dominate, the system forms a QGP.
Then the expanding plasma cools down and below the critical temperature hadrons are created, they form a hadron gas. The temperature of the system decreases further and at the so-called *freeze-out* the hadrons stop to interact.

Nucleon-nucleon reactions are an important baseline for nucleon-nucleus and nucleus-nucleus reactions. Therefore some characteristics of these reactions shall

be mentioned (see e.g. [Won94]). An important quantity for such reactions is the inelastic cross section which is not changing much above center-of-mass energies $\sqrt{s} = 3$ GeV. For example, the inelastic cross section is about 32 mb for $\sqrt{s} = 17$ GeV, about 40 mb for $\sqrt{s} = 130$ GeV and about 42 mb for $\sqrt{s} = 200$ GeV.
About 50 % of the energy of the incoming nucleons is used for particle production, most of the produced particles are pions with a fraction of about 80% to 90% of all produced particles. The remaining 10 to 20 % of particles are other mesons, anti-mesons, baryons and anti-baryons. During this process, the rapidity y of the colliding nuclei changes by about one unity.
The overall number of the particles produced in one collision is given by the multiplicity. For example, the multiplicity for charged particles can be parameterized as

$$\langle N_{ch} \rangle = 0.88 + 0.44 \ln s + 0.118 (\ln s)^2 \ ,$$

where s is given in units of GeV^2.

An important observable is the transverse momentum p_T [1]. The mean transverse momentum of the produced particles is about $\overline{p_T} = 300 - 400$ MeV/c, it only weakly depends on the center of mass energy. The Lorentz invariant cross section $d\sigma/dp_T^2$ [2] as a function of the transverse momentum can be parameterized with an exponential function:

$$\frac{d\sigma}{dp_T^2} \sim \exp(-p_T/T) \ , \ T \approx 160 \text{ MeV} \ .$$

At higher transverse momenta, this function passes over to a power law with the functional form

$$\frac{d\sigma}{dp_T^2} \sim p_T^{-n} \ . \tag{2.1}$$

One possible function following the functional form of 2.1 was proposed by Hagedorn to describe the p_T-dependence of the invariant cross section:

$$\frac{d\sigma}{dp_T^2} = c \cdot (\frac{p_0}{p_T + p_0})^n \text{ [Hag83].} \tag{2.2}$$

The cross section is expected to follow the same functional form for all particle species when regarded as a function of the transverse mass

$$m_T = \sqrt{p_T^2 + m_0^2} \ . \tag{2.3}$$

[1] The transverse momentum and other kinematic variables are explained in appendix A.
[2] see appendix B

The cross sections for different particles will only differ by a constant factor. This is the so-called m_T scaling.
Bjørken predicted that the rapidity distribution exhibits a plateau in the central rapidity region at high collision energies [Bjo83]. At lower energies, the rapidity distribution can be described by a Gaussian.

2.4 QGP Signatures

The formation of a quark gluon plasma has many observable consequences. Most of these observations can be explained by other theoretical approaches by models that do not assume the presence of a QGP. However, it is hoped that the sum of the observations will give evidence for the formation of a QGP. The models explaining one of the observations cannot explain their combined occurrence. An overview of different signatures is given for example in [Har96]:

Kinematic Probes

Thermodynamic variables as energy density, pressure and entropy density as a function of the temperature and the baryochemical potential are often used to describe heavy-ion collisions. The idea to determine them is measuring the average transverse momentum, the hadron rapidity distribution and the transverse energy distribution. Due to the high pressure of the QGP, a collective outward flow is formed during the expansion of the dense matter. Studies on this collective flow can provide information about the equation of state of the hot and dense matter, a modification of the flow is expected during the phase transition.

Electromagnetic Probes

Because photons and leptons are not affected by the strong force, they can leave the interaction region and thus be used to examine the early stages of a heavy ion reaction.
The measurement of direct photons is an important aspect of the PHENIX-experiment. The main source of direct photons are quark-gluon Compton scattering $gq \rightarrow \gamma q$ and quark-antiquark annihilation $q\overline{q} \rightarrow g\gamma$. In a thermal hadron gas, the

main source of photons is the $\pi\rho \rightarrow \gamma\rho$ reaction. Thus a QGP and a hadron gas close to the critical temperature both emit very similar photon spectra. So direct photons alone are not an adequate evidence for a QGP.

Probes of Deconfinement

Another prediction made for a QGP is an enhancement of strangeness, especially the production of multi-strange baryons should show a strong enhancement. In hadronic matter the threshold for strangeness production is fixed by the necessity of the simultaneous production of two hadrons with opposite strangeness. This threshold is about 700 MeV for the most simple reaction $pn \rightarrow \Lambda^0 K^+ n$. In a QGP the threshold for $s\overline{s}$ pair production is about 300 MeV, the double rest mass of the strange quark. Another probe for the quark deconfinement is the suppression of the J/Ψ meson, a bound state of a $c\overline{c}$ pair. The J/Ψ has a high rest mass of about 3.1 MeV and can thus only be produced in hard parton collisions in the early phase of the reaction. The formation of the J/Ψ is suppressed in a QGP because the probability for the $c\overline{c}$ pair to form a bound state is much smaller in a QGP in comparison to a hadron gas. In fact c and $\overline{c}$ are separated and will mostly form D mesons during the hadronization due to the high abundance of u and d quarks.

Probes of Restoration of Chiral Symmetry

The formation of a disoriented chiral condensate (DCC) may be a probe for the restoration of chiral symmetry. The transition from the QGP back to hadronic matter normally leads to the initial state with the chiral symmetry breaking again. If the phase transition proceeds very fast and parts of the plasma cool down rapidly, theoretically an energetically unfavorable state can establish, the DCC. The DCC will lead to a change in the occurrence distribution of neutral versus charged pions which normally is $N_{\pi^0}/N_\pi = 1/3$.
Another effect of the chiral symmetry restoration is a change of the masses and the widths of the light vector mesons as ρ, ω and ϕ compared to the values in cold nuclear matter.

2.5 Jet Quenching

Bunches of particles with high transverse momenta created in particle collisions are called jets. Hard scattering processes are the main source of hadrons with high p_T in proton-proton collisions with collision energies above $\sqrt{s} \approx 50$ GeV [Owe78]. The hadrons are generated in hard parton-parton collisions when the scattered partons fragment into hadrons. They are visible as jets.
Ultrarelativistic heavy ion collisions show a slightly different behavior. The hard processes dominate the particle production at high transverse momenta while soft processes lead to a large background of particles especially at low p_T below ~ 2 GeV. Because hard processes occur in the early phase of the reaction and interact with the hot and dense matter produced in the reaction later on, the produced particle jets provide a good opportunity to study the medium that is created in an ultrarelativistic heavy ion collision. One expectation is the so called jet quenching, the suppression of jet production due to the energy loss of hard scattered partons in hot and dense nuclear matter as a result of gluon bremsstrahlung [Gyu90, Bai95].
The specific energy loss of a parton dE/dz depends on the density of the medium and is proportional to its path length L through the medium [Bai97a, Bai97b]:

$$\frac{dE}{dz} \sim \frac{L}{\lambda_a} \; . \tag{2.4}$$

Here λ_a is the mean free path of gluons in the medium. The total energy loss is proportional to the path length squared: $\Delta E \sim L^2$. This dependency is explained by interference effects according to the Landau-Pomeranchuk-Migdal effect [Lan53, Mig56] in QED. The quark loses energy on its way through the plasma because it emits gluons. With a distance between the scattering centers that is small enough, single or multiple gluons will interfere and the energy loss of the partons will decrease. Thus the total energy loss is smaller than it would be without the interference of the gluons. But the gluons get an additional transverse momentum, so the coherence length decreases and less gluons interfere. This leads to a quadratic dependence of the energy loss on the path length.
Because the identification of single jets is very difficult in heavy ion collisions, another quantity is needed to characterize and quantify possible modifications in particle production at high transverse momenta. The nuclear modification factor R_{AB} [Wan01] gives the opportunity to specify the modification averaged over many events. It is defined as the ratio of the Lorentz invariant hadron multiplicity

$Ed^3N/dp^3(p_T)$ in A+B collisions to the hadron multiplicity in p+p collisions, scaled with the number of inelastic nucleon-nucleon collisions N_{coll} in the A+B collisions:

$$R_{AB}(p_T) = \frac{(E\frac{d^3N}{dp^3}(p_T)/N_{coll})_{AB}}{(E\frac{d^3N}{dp^3}(p_T))_{pp}} \ . \tag{2.5}$$

Here, the nuclei are regarded as an incoherent superposition of partons, so the colliding nuclei are considered a superposition of nucleon nucleon collisions, the so-called binary scaling. R_{AB} should be one for transverse momenta above 2 GeV, for smaller p_T's the biggest part of the particle production scales with the number of participating nuclei, thus R_{AB} is smaller than one in that p_T region.
Jet quenching is not the only effect having an influence on the nuclear modification factor. A comparison of p+p and p+A collisions leads to the observation that collisions of protons and nucleons are not a simple superposition of proton-proton collisions, the cross section behaves like

$$\sigma_{pA} = \sigma_{pp} \cdot A^{\alpha} \text{ with } \alpha > 1 \ . \tag{2.6}$$

This effect is called *Cronin effect* [Ant79], it is explained by multiple soft scattering of the incoming partons before the hard collision.
Other effects having smaller impact on the particle production at high p_T are nuclear effects in parton distribution functions (PDF) [Per90]. The probability of finding a parton with momentum fraction x is given by the PDF $F_2(x, Q^2)$. This function is different in nuclei ($F_2^A(x, Q^2)$) and in free nucleons ($F_2^p(x, Q2)$) as measured in deeply inelastic scattering experiments [Pil00]. There are different effects for nuclear effects described by $R_F = F_2^A/F_2^d$, using the PDF of deuterium $f_2^d(x, Q^2)$ as an approximation to the average structural function of nucleons; they have been detected in different experiments.

$R_F < 1$:	nuclear shadowing	for $0.0 \lesssim x \lesssim 0.1$
$R_F > 1$:	anti-shadowing	for $0.1 \lesssim x \lesssim 0.2$
$R_F < 1$:	EMC effect	for $0.3 \lesssim x \lesssim 0.8$
$R_F > 1$:	Fermi motion	for $x \to 1$

Another possible explanation for a modification of R_{AB} is the possible formation of a so-called Color Glass Condensate in the incoming nuclei [Ian03]. This initial state effect could be responsible for a suppression of the particle production at $\sqrt{s_{NN}} = 200$

GeV heavy ion collisions and would have a similar effect on the particle production in p+A or d+A collisions.

3 The PHENIX Experiment

The PHENIX experiment is one of four experiments located at the Relativistic Heavy Ion Collider (RHIC). It aims at measuring hadrons, leptons and photons from collisions of two nuclei, proton and nucleus or two protons. These measurements shall provide evidence for a quark-gluon plasma possibly created in central collisions of heavy nuclei. The experiment also shall study the physical properties of the state of matter created in such events. RHIC provides polarized proton beams which enables PHENIX to study the spin structure of the nucleon in addition to collisions of heavy ions.
Overviews of the PHENIX experiment and the RHIC facility can be found for example in [Bat02, Bus02, Mer00].

3.1 The Relativistic Heavy Ion Collider

RHIC [Hah03], located at Brookhaven National Laboratory (BNL), is the first hadron collider with two independent rings. Its major construction was finished in 1999. Both rings have a circumference of 3.8 kilometers, they cross at 6 interaction points where the particle beams can collide. Figure 3.1 gives an overview over the RHIC complex.
At RHIC it is possible to accelerate heavy nuclei as well as light nuclei and polarized protons. The collider provides the opportunity to accelerate different particle types in the two rings. The beam energy can be varied over a large range. The maximum beam energy depends on the mass of the accelerated particles, it is 100 AGeV for gold nuclei and 250 GeV for protons. As RHIC is a collider, the entire energy of the two beams is converted into collision energy. Thus the maximum center of mass energy is 200 AGeV for Au+Au and 500 GeV for p+p collisions. The design luminosity of the collider is $2 \times 10^{26}\mathrm{cm}^{-2}\mathrm{s}^{-1}$ for 200 AGeV Au+Au collisions.
The beam is produced in one of the pre-accelerators. The Tandem van de Graaff accelerates Au^{-1} ions from a pulsed sputter ion source to an energy of about 1 AMeV, the electrons are stripped away on their way to the booster and to the Alternat-

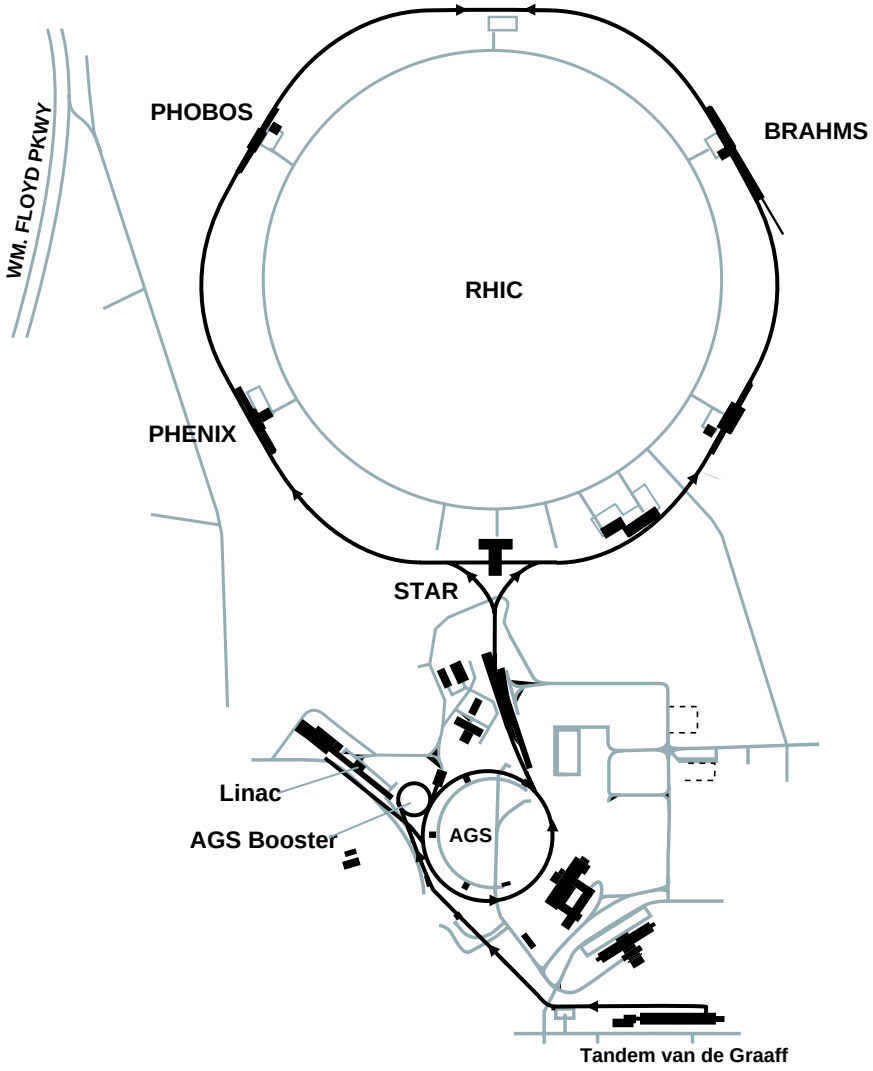

Figure 3.1: Schematic view of the Relativistic Heavy Ion Collider at BNL with the pre-accelerators (according to [Hah03]).

ing Gradient Synchrotron (AGS). Protons are supplied by the Linear Accelerator (Linac), they are injected into the booster accelerator and then into the AGS as well.

3.2 Experiments at RHIC

Four experiments are located at RHIC, the two bigger experiments STAR[1] and PHENIX and the two smaller experiments PHOBOS and BRAHMS[2]. Two of the interaction points are not used at present, future experiments could be installed there. The experiments have their main focus on different aspects of the search for the QGP, each of them is constructed for very exact measurements of certain variables and less accurate measurements of other variables.

3.2.1 STAR

The STAR experiment [Ack03] is specialized in reconstructing the tracks of several thousand particles produced in heavy ion collisions at RHIC. It measures the hadron production and studies global observables which are correlated for single events to look for signals of the QGP. Therefore STAR measures inclusive η and p_T distributions of charged particles. As STAR has a large acceptance, the experiment is well suited for event-by-event characterizations of heavy ion collisions and for the detection of hadron jets.
The most important part of the STAR detector is a large time projection chamber (TPC) which is placed inside a solenoid magnet. STAR is also designed to analyze the photon and pomeron interactions from electromagnetic fields of the passing ions in ultraperipheral reactions.

3.2.2 PHOBOS

PHOBOS [Bac03] consists of a large number of silicon detectors which surround the collision point nearly completely, so the experiment can measure the multiplicity of

[1] Solenoidal Tracker At RHIC
[2] Broad RAnge Hadron Magnetic Spectrometers

charged particles. PHOBOS can detect particles with very low transverse momenta because the material between the collision vertex and the first layers of detectors has been minimized.
A two-arm spectrometer included in PHOBOS allows a detailed analysis of about 2 % of the particles produced in each collision. These spectrometers cover the midrapidity range ($0 \leq \eta \leq 2$) where the highest energy densities and interesting physics effects are expected to occur.

3.2.3 BRAHMS

BRAHMS [Ada03] is designed to measure the production of charged particles as a function of the transverse momentum and the rapidity. Therefore the experiment has two moving spectrometer arms, one located at midrapidity, the other one in forward direction. By varying their position, BRAHMS can measure the particle production depending on the pseudorapidity. With the help of its tracking detectors, time-of-flight arms and Čerenkov detectors, it can determine particle momenta and identify particles over a wide range of rapidity and transverse momentum.
Physics goals of BRAHMS are mapping out the rapidity density distribution for protons and antiprotons, the spectroscopy of kaons and pions and light clusters as deuterons and anti-deuterons.

3.3 Construction of PHENIX

The PHENIX experiment [Adc03a] is designed for the measurement of many different particle species as photons, electrons, charged hadrons and muons at high rates in one experiment. Thus the experiment consists of several different detectors. Basically, the experiment consists of two different spectrometers. The central spectrometer, divided in two arms, provides the measurement of hadrons, photons and leptons at midrapidity. Muons in forward direction are measured by a muon spectrometer that has two arms as well. Besides these two spectrometers there are also detectors for global event characterization at PHENIX. Since the subject of this thesis is a measurement at PHENIX, the PHENIX detectors will be described in the following sections. The PHENIX experiment is shown in the Figures 3.2 and 3.3.

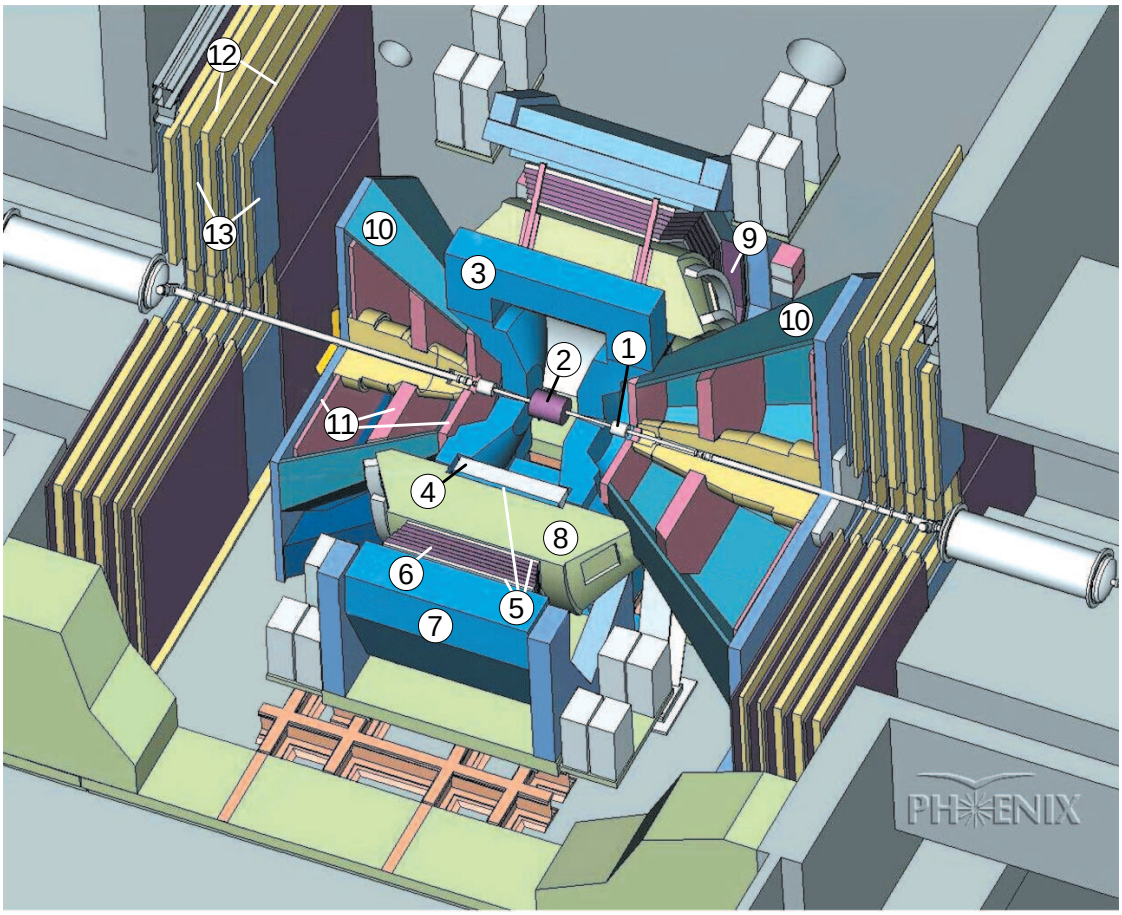

Figure 3.2: Schematic view of the PHENIX experiment: **1.** Beam Beam Counter (BBC), **2.** Multiplicity Vertex Detector (MVD), **3.** Central Magnet (CM), **4.** Drift Chamber (DC), **5.** Pad Chambers (PC), **6.** Time Expansion Chamber (TEC), **7.** Electromagnetic Calorimeter (EMCal), **8.** Ring Imaging Čerenkov Detector (RICH), **9.** Time of Flight (TOF), **10.** Muon Magnets (MM), **11.** Muon Trackers (μT), **12.** Absorber Plates, **13.** Streamer Tubes.

3.3.1 Global Detectors

The global detectors are the two Beam-Beam Counters (BBCs), the Multiplicity Vertex Detector (MVD), the two Zero Degree Calorimeters (ZDCs) and the forward calorimeters.

The two identical parts of the **BBC** are located at both sides of the collision region, their distance to the collision point is $z = \pm 144$ cm. Both BBC detectors have 64 elements which consist of quartz Čerenkov radiators, each of them is read out by a photomultiplier. The detectors measure the time of flight of particles in the rapidity range $3.1 < |y| < 3.9$ to determine the time and the location of the collision.

The **ZDC** consists of two identical parts located at a distance of $z = \pm 18.25$ m along the beam axis from the collision point. The ZDC detects particles in a small angular region of $\theta < 2$ mr. As neutrons are not deflected by the magnetic field because they are not charged, the ZDC can measure spectator neutrons from ion-ion collisions. The difference between the time signals of the two detectors can be used to determine the vertex point, the ZDC signal is also used for the centrality determination. The ZDC consists respectively of three modules, each $2\lambda_{had}$ [3] deep and read-out by a photomultiplier. Each RHIC experiment uses the same type of ZDCs, so the results can be compared by the global measurement category E_F which is the energy in forward direction.

The **MVD** surrounds the collision point, covering the pseudorapidity range of $-2.64 < \eta < 2.64$ in full azimuth. It is a highly segmented silicon detector consisting of a structure of Si-bands and Si-pads. The MVD measures the vertex position with high precision as well as the particle multiplicity and its distribution in pseudorapidity and azimuth.
A more detailed description of the BBC, the ZDC and the MVD is given in [All03].

3.3.2 The Central Spectrometer

Several different detectors are part of the central spectrometer, they have the ability to measure different particle species as electrons, photons and charged hadrons. The central spectrometer covers the pseudorapidity range $|\eta| < 0.35$, each of its arms

[3] λ_{had} denotes the hadronic interaction length

covers 90 degree in azimuth. Because of their location towards the beam axis, the arms are called east arm and west arm. Most of the detectors described in the following can be found in both arms.

The **Central Magnet**, weighing 421 tons, creates an axial magnetic field around the beam axis with a maximum field integral of 1.15 Tm. The field drops strongly outward because it must not disturb the measurement of the RICH detector. The magnetic field bends charged particles in the plane perpendicular to the beam axis. More information about the magnet system is given in[Aro03].

At the edge of the magnetic field, both arms have a **Drift Chamber** for charged particle tracking. Its radial difference to the beam axis is 2.02 m $<$ r $<$ 2.46 m. The momentum of the particle can be calculated from the curvature of the track in the magnetic field.

Next to the drift chambers there is a first **Pad Chamber** (PC1) in both arms. It is read out via pads with a size of 8.45×8.40 mm^2. The pads give the cross-over point of a particle track with the detector plane. This first pad chamber and the drift chamber are used for particle tracking in the inner region of the central spectrometer directly behind the strong magnetic field.

The pad chambers are followed by the **Ring Imaging Čerenkov Detector** (RICH), which covers the radial range of 2.5 m $<$ r $<$ 4.0 m. The RICH covers a volume of 40 m^3 in each arm and has an entrance window of 8.9 m^2 and an exit window of 21.6 m^2. RICH, a threshold Čerenkov detector, is used for identifying electrons. Electrons with a momentum $p > 18$ MeV emit Čerenkov light in the gas radiator while pions with momenta $p < 4.9$ GeV do not generate a signal in the detector. The Čerenkov light is focused on photomultipliers by thin mirrors.

Another **Pad Chamber** (PC 2) is located behind the RICH at $r = 4.19$ m in the western arm. The pads in the second pad chamber have a size of 14.24×13.55 mm^2, this gives the PC 2 the same resolution in space as the PC 1.

In the east arm, there is a **Time Expansion Chamber** (TEC) outside the RICH. It has four wire layers, its distance to the beam axis is 4.23 m $<$ r $<$ 4.88 m. The TEC provides two dimensional tracking in the x-y plane. With the measurement

of dE/dx it helps identifying pions and electrons. In combination with the DC it improves the momentum resolution for particles with high transverse momentum.

At a radius of $r = 4.90$ m there is a third **Pad Chamber** (PC3), with a pad size of 16.7×16.0 mm^2. The TEC, the DCs and the PCs are described in detail in [Adc03b].

A **Time-of-Flight** detector (TOF) is located behind a part of the third pad chamber in the east arm. This detector consists of 960 plastic scintillators that are read-out by photomultipliers at both ends. The scintillators are placed in $r - \theta$ direction. The TOF helps identifying particles in combination with the tracking detectors, also the longitudinal position of a particle on the scintillator is measured. The Time-of-Flight as well as the RICH are described in [Aiz03].

The **Electromagnetic Calorimeter** (EMCal) completes the central arm. Behind the TOF detector, a lead glass calorimeter is located. A lead scintillator calorimeter is located behind the third pad chamber in the upper part of the east arm and in the west arm. The EMCal will be introduced in section 3.4, a more detailed description can be found in [Aph03a].

3.3.3 The Muon Spectrometer

The muon spectrometer consists of two arms in both longitudinal directions. It detects and tracks muons in the forward rapidity range $1.1 < |\eta < 2.4$. The muon spectrometer allows the measurement of the vector mesons like Ψ', J/Ψ and Υ. For example, the J/Ψ decays into a muon/antimuon pair. Both arms consist of a muon tracker and a muon identifier, they cover the full azimuthal angle.

The **Muon Trackers** (μTR) contain magnets that create a radial field, they open funnel-shaped from the interaction region along the beam line. Three drift chambers at their front edge ($z = \pm 1.60$ m), in their middle ($z = \pm 3$ m) and at their rear edge ($z = \pm 4.60$ m) are used for the tracking of the particles.

The **Muon Identifier** (μID) is located behind the muon magnets in both arms. Consisting of six steel armored absorber plates, alternatingly coated with streamer tube detectors, the μID measures almost exclusively (99.9 %) muons because the absorbers suppress pions and kaons very strongly. The detector cannot measure

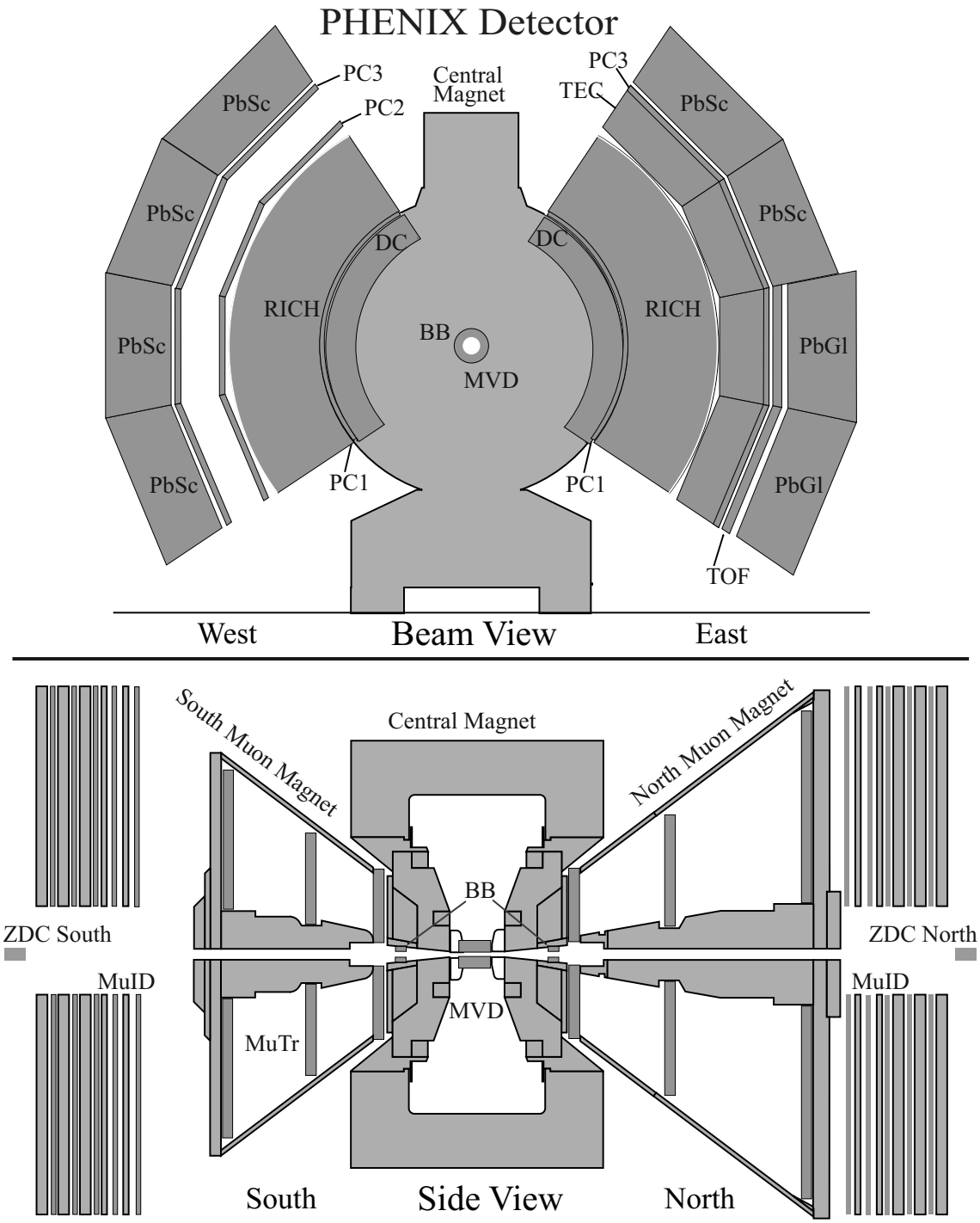

Figure 3.3: The PHENIX experiment in 2003.

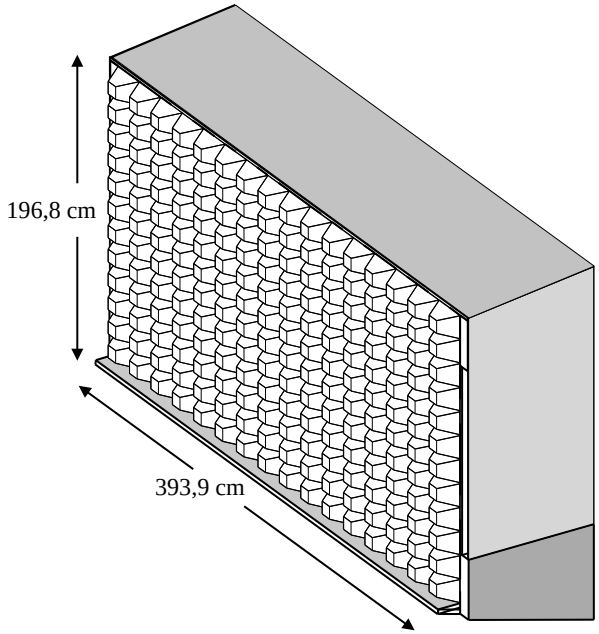

Figure 3.4: One of the two PbGl detectors.

muons with an energy lower than 1.9 GeV as they are suppressed as well. The muon spectrometer is introduced more specific in [Aki03].

3.4 The Electromagnetic Calorimeter

The **Electromagnetic Calorimeter** (EMCal) is designed for measuring the energy and the position of photons and electrons in midrapidity range ($|\eta| < 0.7$) over an azimuthal angle of π. The calorimeter consists of eight sectors, each covering $\pi/8$ in azimuth. The EMCal consists of two different detectors, a lead glass detector (PbGl) with two sectors and a lead scintillator detector (PbSc) with six sectors. Both detectors have a very good resolution in space, time and energy. With the help of the time-of-flight signal of the detector in combination with the measurements of the tracking detectors, charged particles can be identified.

3.4.1 The Lead Glass Detector

The lead glass detector in PHENIX is composed of the LEDA[4] detector from the WA98 experiment at CERN. LEDA has been geometrically rearranged to be installed at PHENIX.
Both sectors of the lead glass detector consist of 12 × 16 supermodules each with 4 × 6 modules. Each of the lead glass modules has a size of 4 × 4 ×40 cm^3 big and is read out by a photomultiplier. The total number of read-out channels is 9216. The photomultipliers detect the Čerenkov photons that are generated by electrons from electromagnetic showers.
Each supermodule has its own reference system which consists of three light emitting diodes at the front side of the supermodules. These LEDs emit light imitating different characteristics of the Čerenkov light which is generated in the detector, so that gain fluctuations can be detected. The LEDs are again controlled by a photo diode to compensate for aging effects.

3.4.2 The Lead Scintillator Detector

The six lead scintillator sectors are composed of 6 × 3 supermodules containing 6 × 6 modules each. The modules contain four optically separated towers. The 15552 towers of the six sectors cover an area of about 48 m^2. The PbSc is a sandwich calorimeter consisting of alternating layers of lead absorbers and scintillator plates that are read out by optical fibers.
Each module consists of scintillator layers built of four identical plates, so each tower has an own scintillator plate in each layer. Each plate has 36 holes for optical fibers which connect the scintillator plates. The towers have 2 × 18 fibers, each of them crosses the tower twice and is read out by a photomultiplier at both of its ends.
As a reference signal, light from a YAG laser is injected in each module with the help of an additional fiber in the middle of the module. This reference acts as a control for gain fluctuations in the detector.

[4]LEad glass Detector Array

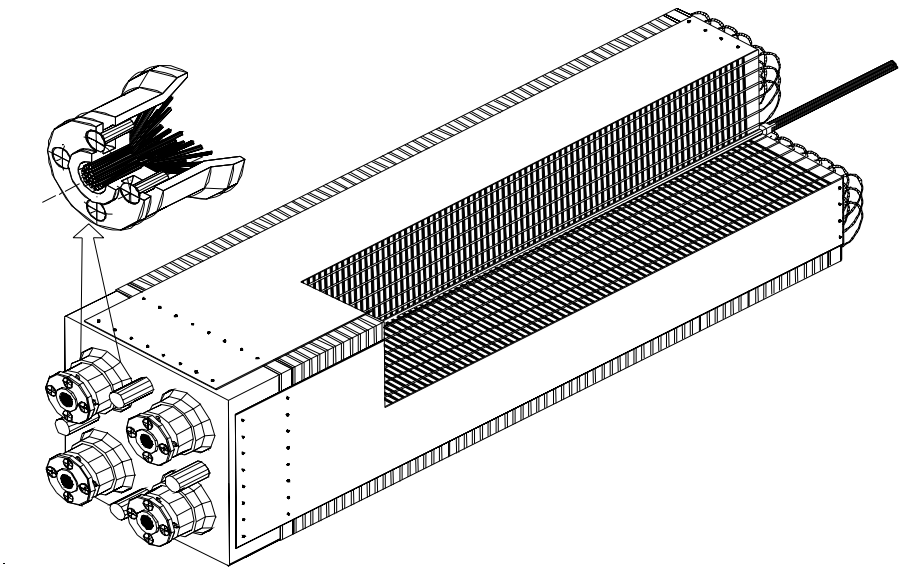

Figure 3.5: A module of the Lead Scintillator detector.

4 Measurement of η Mesons in PHENIX

The analysis of the production of π^0-mesons in p+p, d+Au and Au+Au collisions at RHIC has lead to interesting results. A strong suppression of the π^0-production compared to the p+p reference has been observed in central $\sqrt{s_{NN}} = 200$ GeV Au+Au collisions at RHIC [Adl03a] while there is no suppression in d+Au collisions at the same energy [Adl03b]. The PHENIX experiment has also measured the production of protons in central Au+Au collisions where no suppression occurs for the measured p_T range up to $p_T = 4.5$ GeV/c [Adl03d].
The η meson is produced in collisions at RHIC, too, and because of its decay $\eta \to \gamma\gamma$ it can be measured with the EMCal. The analysis is similar to the π^0 measurement which uses the decay $\pi^0 \to \gamma\gamma$.
The measurement of the η can shed light on the particle species dependence of the nuclear modification factor. Another important result is the ratio of η and π^0 in ultrarelativistic collisions. This ratio is e.g. needed in the analysis of direct photons in such reactions.

4.1 The η Meson

The η meson is a light unflavored pseudoscalar meson with a mass of 547.30 ± 0.12 MeV and a width of $\Gamma = 1.18 \pm 0.11$ keV [Hag02]. It can be described as $\eta \approx \frac{1}{\sqrt{6}}(u\overline{u} + d\overline{d} - 2s\overline{s})$. The main decay modes of the η are neutral modes as the already mentioned $\eta \to \gamma\gamma$ decay. This decay has a branching ratio of (39.43 ± 0.26) % . Another neutral modes is the $\eta \to 3\pi^0$ decay $(32.51 \pm 0.29$ %). The most important charged decay modes are $\eta \to \pi^+\pi^-\pi^0$ $(22.6 \pm 0.4$ %) and $\eta \to \pi^+\pi^-\gamma$ with a branching ratio of $(4.68 \pm 0.11$ %). The other decay modes have much smaller branching ratios.

4.2 Analysis of the PHENIX Data

The raw data measured by the PHENIX electromagnetic calorimeter have to be converted into physical information as e.g. energy and position of each calorimeter hit first. For this analysis, about 59.2 million minimum bias events in d+Au collisions and about 22.5 million minimum bias events in p+p collisions taken in the third experimental run (Run 3) have been used.

4.2.1 Calibration of the EMCal

The basic principle used for the calibration of the EMCal is the measurement of particles of known energy. The measured data are compared to the known attributes of this test-beam.
A test-beam measurement performed at the AGS showed that minimum ionizing particles produce a 260 MeV signal in the PbSc calorimeter [Baz02]. These minimum ionizing particles can be used to obtain an initial calibration. A better test of the energy scale is performed by looking at electrons. The momenta of electrons are measured with the drift chamber, these electrons with known momentum lead to an electromagnetic shower in the EMCal. Because the total energy of such showers is known, they can be used to calibrate the calorimeter.
The LED system of the lead glass calorimeter is also used to obtain time dependent gain corrections. The LEDs emit light with known intensity, so gain fluctuations can be detected.
As the methods described above have too large errors, the final calibration is obtained by comparing the measured peak position of the π^0 to expected values. To this end, π^0 spectra are measured with a sharp asymmetry cut, so that the π^0 energy is proportional to the energy of the decay photons.

4.2.2 Photon Identification

The analysis leading to fully corrected η spectra is performed for different methods of photon identification (PID). Therefore two different photon identification cuts are used. These cuts reduce the background from hadrons, but they also lower the number of photons that will be analyzed. The two applied cuts lead to four dif-

ferent photon identification methods as the cuts can be combined. The energy cut only accepts photons above a certain energy threshold while the shower shape cut will reject detector signals resulting from broad showers which are mostly hadronic showers. The four different PIDs used in the analysis are

- no PID cut (PID 0)
- cut on the energy of the cluster (PID 1)
- cut on the shower shape (PID 2)
- cut on the energy and the shower shape (PID 3)

All methods should yield the same result when the efficiency corrections for the different methods are applied. Differences in the results can help estimating systematic errors for the η spectra.
The basic principle for the shower shape cut is the observation that hadronic and electromagnetic showers have different lateral shower profiles in the calorimeter. In the PbSc calorimeter a cut on χ^2 is used. The showers are therefore compared to a photonic shower shape of the cluster. This photonic shower shape is based on an analytical parameterization of the energy sharing and its fluctuations. In the PbGl calorimeter the angular dependent dispersion of a cluster is determined to perform the shower shape cut.
As photons are moving faster than hadrons - e.g. the proton - with a high rest mass, a time-of-flight cut can also help to reject EMCal signals from incoming hadrons. As the time-of-flight cut is mostly equivalent to an energy cut, the TOF cut was replaced by a moderate energy threshold of 0.2 GeV.

4.2.3 High p_T Events

The spectrum above a transverse momentum of $p_T = 3.5$ GeV/c is determined from events accumulated with the EMCal RICH Trigger (ERT). The use of the ERT leads to an extension of the η p_T spectrum to high p_T.
In the analyzed d+Au and p+p runs, the ERT 4x4 is used. This trigger is sensitive on the sum of the signals of 4x4 EMCal towers, so-called 4x4 trigger tiles. These tiles overlap to avoid inefficiencies at their edges. Each 2x2 tile belongs to four different

4x4 tiles. The trigger can use three different setups that differ in the energy threshold. In the analysis of d+Au events, the *Gamma1* (G1) trigger was used for the high p_T sample while the *Gamma3* (G3) trigger was used in p+p events. The two triggers use different trigger thresholds, 2.1 GeV for the G1 trigger and 1.4 GeV for the G3 trigger.
The ERT triggered events can only be used to extend the minimum bias p_T spectrum when they have been corrected for the additional bias which is obviously caused by the ERT. To determine the correctly normalized η spectrum for ERT triggered events, one defines

$$\varepsilon_{evt}^{ERT} = \frac{N_{evt}(mb \wedge ERT)}{N_{evt}(mb)} \tag{4.1}$$

$$\varepsilon_{\eta}^{ERT} = \frac{N_{\eta}(mb \wedge ERT)}{N_{\eta}(mb)} \tag{4.2}$$

using the minimum bias sample. So when measuring the ERT triggered sample, one can obtain the total number of underlying minimum bias events and the total number of η's:

$$N_{evt}^{mb} = \frac{1}{\varepsilon_{evt}^{ERT}} \cdot N_{evt}(ERT) \tag{4.3}$$

$$N_{evt}^{\eta} = \frac{1}{\varepsilon_{\eta}^{ERT}} \cdot N_{evt}(ERT) \tag{4.4}$$

4.2.4 Centrality Determination

The events in d+Au collisions are classified into four different centrality classes which allow to study possible centrality dependences of the particle production. In central events, the number of nucleon-nucleon collisions is larger than in peripheral events, so the energy density is higher in central collisions. The determination of the centrality is described in [Dre03, Bat03].
To determine the centrality classes in d+Au events, the response of the southern Beam-Beam Counter (BBCS), i.e. the Au-going side, is related to the number of participants in the gold nuclei (see [Dre03]). Therefore the number of observed hits in the BBCS has to be proportional to the number of participants in the gold nucleus. The distribution of the normalized charge in the BBCS and the classification into the centrality classes is shown in Figure 4.1.

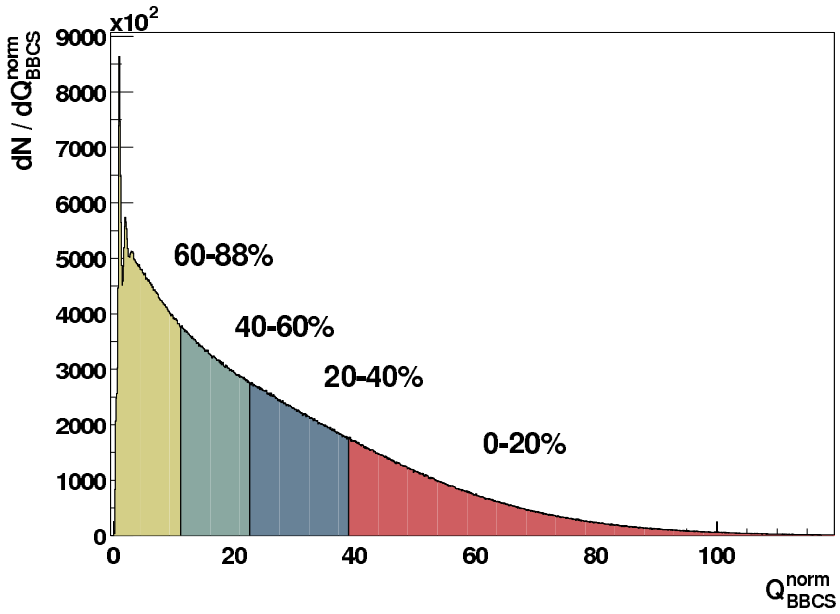

Figure 4.1: Distribution of the normalized charge in the southern Beam Beam Counter (BBCS). The normalization is done in a way that the normalized charge corresponds to the number of hits. [Bat03]

4.3 η Measurement

The measurement of the η mesons is performed in two main steps. First, the raw η signal is extracted from invariant mass spectra for different transverse momenta. In a second step, the raw spectra are corrected e.g. for geometric acceptance and reconstruction efficiency of the detector to get the real spectrum.
The lifetime of the η meson is related to its width and is $\tau \approx 5.578 \cdot 10^{-19}$ s, so $c\tau = 0.167$ nm. Thus the particle decays nearly at the vertex point of the collision and its momentum can be identified by measuring the energies of the decay photons and their position in the electromagnetic calorimeter. The momentum of the η is the vector sum of the two photon momenta.
It is not possible to assign the measured photons to an η because too many photon hits are produced in each collision. Therefore one needs to calculate the relativistic invariant mass of every possible photon pair combination. The invariant mass is

$$m_{inv}^2 = (E_1 + E_2)^2 - (\vec{p}_1 + \vec{p}_2)^2 \ , \tag{4.5}$$

and because of the zero rest mass of the photons, the invariant mass can be calculated as

$$m_{inv}^2 = 2E_1E_2(1-\cos\theta) \ . \tag{4.6}$$

Here, θ is the angle between the two photons. Photon pairs belonging to real η mesons will have an invariant mass of about 547.3 GeV/c^2, but there will be photon pairs with the same invariant mass by coincidence because every possible photon pair is considered. An asymmetry cut is applied to improve the signal to background ratio. In the analysis, the background has to be subtracted, the so-called event mixing provides a good method to do so.

4.3.1 Asymmetry Cut

The asymmetry describes the difference between the energies of the two decay photons. It is defined as

$$\alpha = \left|\frac{E_1 - E_2}{E_1 + E_2}\right| \tag{4.7}$$

where E_1, E_2 denote the photon energies. Decay photons from an η decay exhibit a flat asymmetry distribution.
This is different for uncorrelated photon pairs. The single photon spectrum follows roughly a falling exponential function, so each high energetic photon is combined with lots of low energy photons. Cutting off pairs with an asymmetry higher than a certain value will discard such pairs. Of course some correlated pairs will disappear because of the cut, but at high asymmetries the fraction of uncorrelated pairs is much larger. Hence the statistical error will fall with the enhancement of the correlated-uncorrelated pair ratio, otherwise the statistical error will grow due to the cut off of correlated pairs.
The experience of earlier analyses has shown that an asymmetry cut of $\alpha < 0.7$ yields the optimal signal to background ratio. The loss of η's because of the asymmetry cut is corrected during the acceptance and efficiency corrections.

4.3.2 Event Mixing

Photons from different events cannot be correlated. Thus pair combinations with two photons from different events give a distribution of uncorrelated pairs which is similar

to the combinatorial background of the pairs from real events. They can be used to estimate the background. Therefore photons from the current event are combined with photons from earlier events, one gets a so-called mixed event distribution of uncorrelated photon pairs.

4.3.3 η Peak Extraction

To extract the η signal from the invariant mass spectra of the photon pairs, first the combinatorial background has to be subtracted. The mixed event spectrum is scaled with a function describing the ratio of the real spectrum and the mixed event spectrum outside the peak region. Then the scaled mixed event spectrum is subtracted from the real event spectrum. After this background subtraction, the invariant mass spectrum is integrated in the expected η peak region. These steps are performed for different p_T-intervals. The details are described in the following pages.

Background Subtraction

The combinatorial background which is estimated with the event mixing method has to be subtracted from the invariant mass spectrum of real events. Therefore the mixed event distribution has to be normalized to the real invariant mass spectrum, because the number of pair combinations will be different in real and mixed events. In real events, there are $\frac{n_{\gamma,i} \cdot (n_{\gamma,i}-1)}{2}$ photon pairs, while the event mixing leads to $n_{\gamma,i} \cdot n_{\gamma,j}$ pair combinations per event. With n mixed events, the normalization factor will be about $1/2 \cdot n$. To estimate the scaling of the background, first of all the distribution of the real events is divided by the mixed event distribution. This ratio is shown in the upper part of the Figures 4.2 and 4.3. One can see a peak at about 550 MeV, the mass of the η meson. The scaling function is estimated by a fit in the region outside the peak, therefore the spectrum is fitted by a second degree polynom in the region represented by the vertical lines in the upper and the middle part of the Figures 4.2 and 4.3.
The background is parameterized with a second degree polynom because it falls from lower to higher invariant mass values and because it has a slight curvature. To ensure that the fit does not result in a positive curvature of the parameterization function which would not agree with the observations, the corresponding parameter

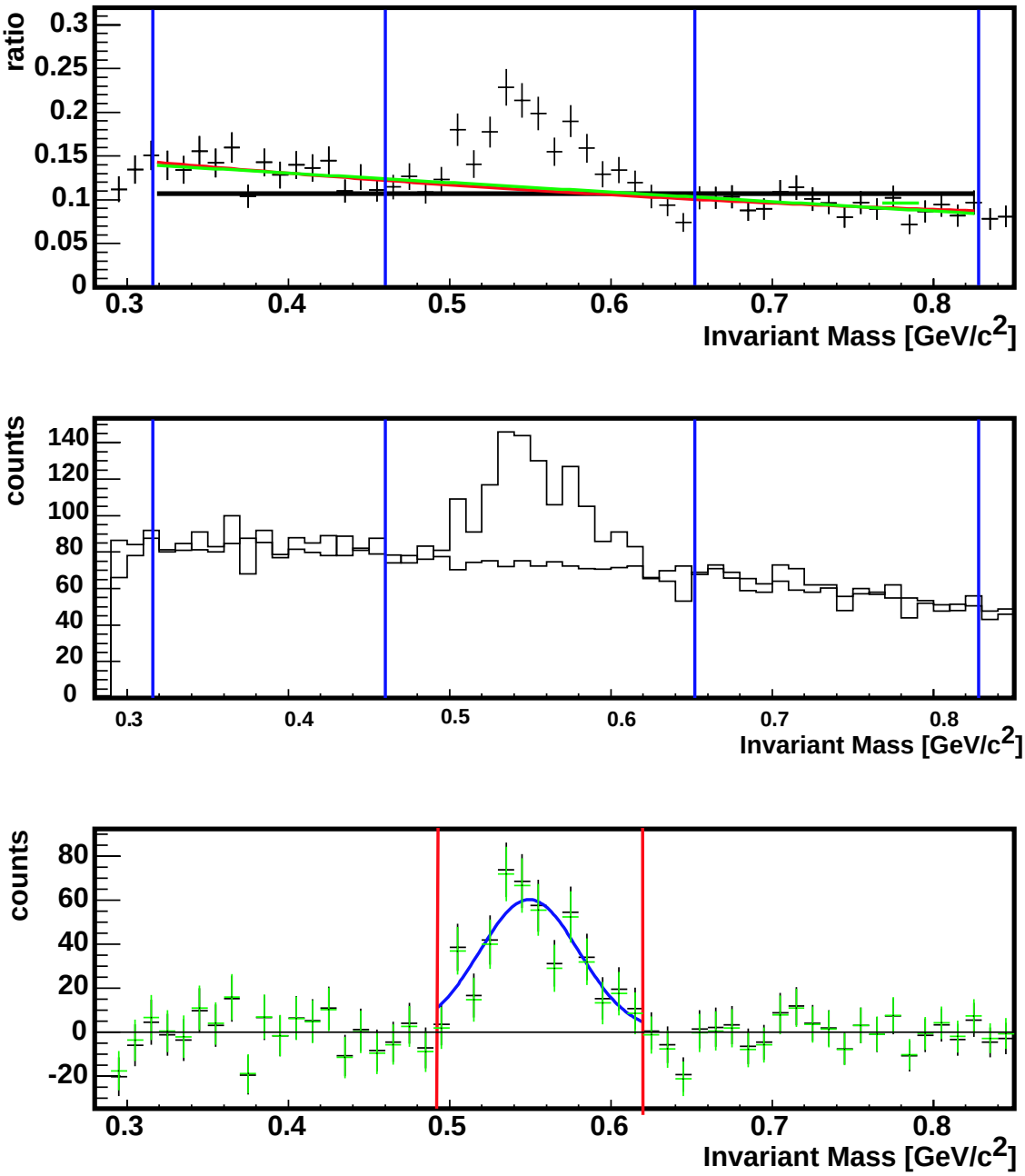

Figure 4.2: Control output of the peak extraction for d+Au min bias events in the range 3.5 GeV/c $< p_T <$ 4.0 GeV/c for PID 3. Top: real-mixed-ratio and background fit, the red fit is used for the background parameterization, the green fit for estimating the systematic error; middle: real invariant mass spectrum and scaled background; bottom: real - scaled background (black entries), the green entries result from the background fit for estimating the systematic error.

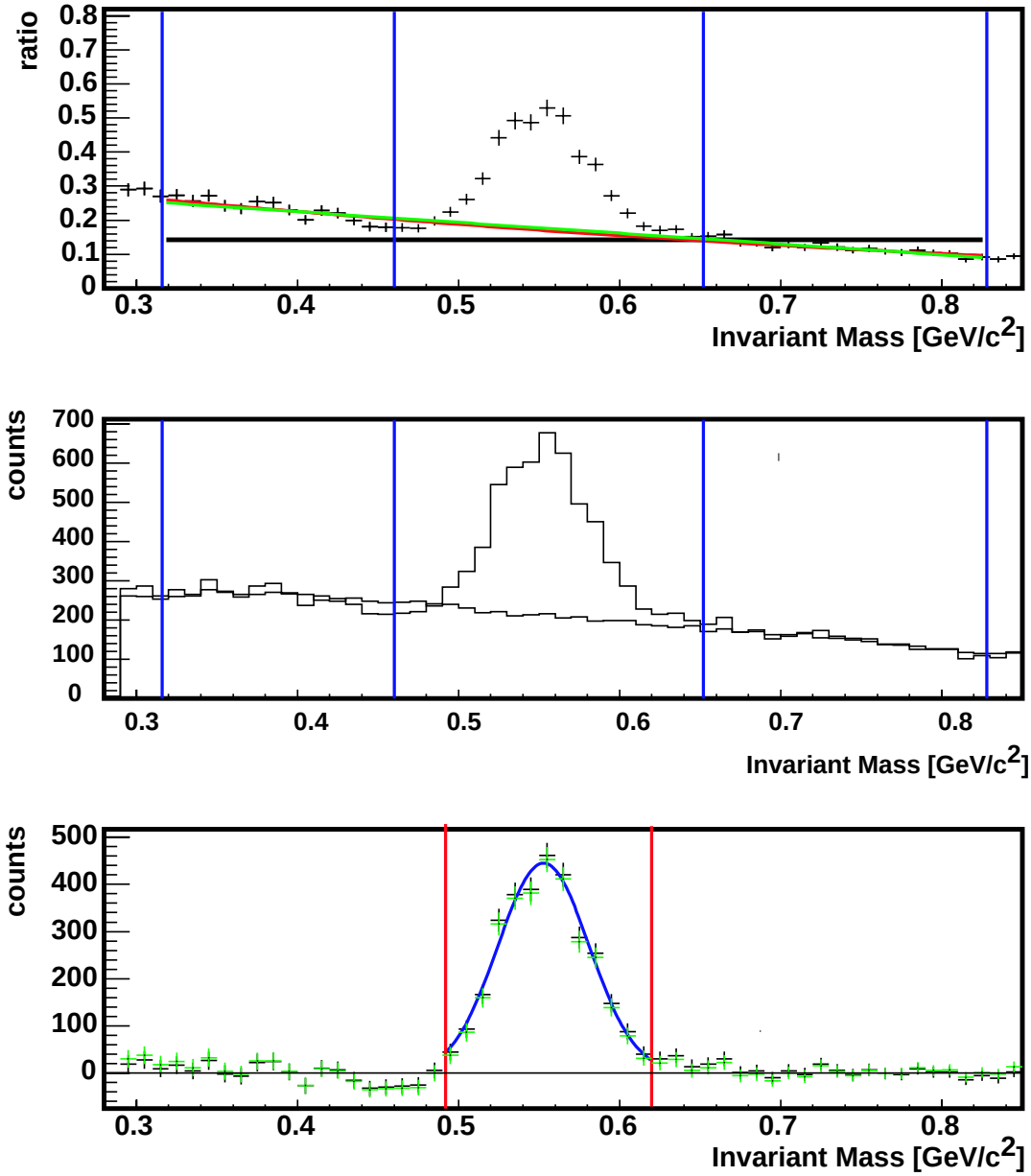

Figure 4.3: Control output of the peak extraction for p+p G3-triggered events in the range 4.0 GeV/c $< p_T <$ 4.5 GeV/c for PID 3. Top: real-mixed-ratio and background fit, the red fit is used for the background parameterization, the green fit for estimating the systematic error; middle: real invariant mass spectrum and scaled background; bottom: real - scaled background (black entries), the green entries result from the background fit for estimating the systematic error.

is limited to negative values. The used fit is not very different to a fit with a linear function, but it describes the spectrum slightly better.
The interval of the background adjustment is limited by two input parameters: the expected peak position m and width σ. Both were estimated in a first analysis of the spectra and set to $m = 556$ MeV/c^2 and $\sigma = 32$ MeV/c^2. The interval now includes the region between $m - 7.5\sigma$ and $m + 8.5\sigma$ (316 MeV/c^2 and 828 MeV/c^2). The peak region $m \pm 3\sigma$ ($460\text{MeV/c}^2 < \text{m}_{\text{inv}} < 652\text{MeV/c}^2$) is excluded.
The average peak position in the invariant mass spectra is about 9 MeV larger than the mass of the η meson. The measured peak position is affected by detector effects which lead to energy smearing. Especially the energy resolution of the detector and the finite size of energy bins lead to a smearing of measured photon energies. This energy smearing widens the η signal. It also shifts the average measured energy of the decay photons to a higher value due to the exponential single photon spectrum. For higher transverse momenta, the background almost vanishes and so the estimation of the scaling by a fit leads to large errors. Hence an alternative method to estimate the background scaling is used for large transverse momenta. The fit function is replaced by the ratio of the number of photon pairs in the normalization region in the real and the mixed events distribution.
The mixed events distribution is scaled with the parameterized fit function - or, in case of large transverse momenta, with the constant as described above - and then subtracted by the real events distribution. The real events distribution and the scaled mixed events distribution are shown in the middle part of Figures 4.2 and 4.3, the vertical lines denoting the interval for the fit function. The final real event distribution after the background subtraction is at last shown in the lower part of the Figures 4.2 and 4.3.

Counting the η's

Another predefined interval is used to count the number of η mesons in each p_T interval. Therefore the integral of the invariant mass distribution after the background subtraction is calculated in the interval $[m - 2\sigma; m + 2\sigma]$. The values of m and σ are the same as used above, so the range of the interval is from 492 MeV to 620 MeV. The size of this interval has to be regarded in the following corrections as well.

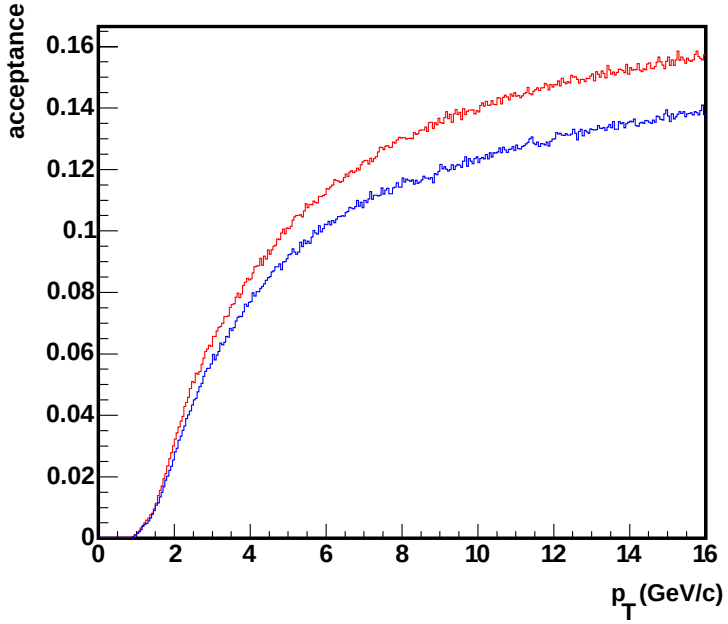

Figure 4.4: Geometric acceptance for the η meson in both d+Au (red) and p+p (blue) collisions at PHENIX in Run 3.

4.3.4 Corrections

The spectrum resulting from the peak extraction has to be corrected to represent physical results. The amount of η's which can principally be detected due to the geometry of the detector is described by the geometric acceptance; the reconstruction efficiency describes the ability of the detector to measure a photon hitting its surface. A bin-shift correction is necessary because of the steeply falling spectrum of η's; effects of the detectors between the vertex point and the EMCal are taken into account by the conversion correction.
The acceptance as well as the efficiency is calculated with a fast monte carlo (fastMC) simulation using routines from the programming library Jetset [Sjo94]. The Jetset library is used to simulate the decay of the η.

Acceptance Correction

The geometric acceptance describes which fraction of produced η mesons will hit the detector due to the solid angle the detector covers. A decay photon will be accepted by the detector in the fastMC when it hits the active surface of the detector

covering the rapidity range $-0.45 < y < 0.45$ and π in azimuth. The acceptance shows a strong dependency on the transverse momentum because the opening angle of the decay photons rises with decreasing p_T. Thus the probability that both decay photons hit the detector decreases for small values of p_T. The acceptance for p+p and d+Au collisions is shown in Figure 4.4. The acceptance is influenced by the geometry of the whole detector as well as by dead and hot modules.

Efficiency Correction

The reconstruction efficiency takes into account that the measured output spectrum is different from the physical input spectrum, thus the reconstruction efficiency is defined as the ratio between the output and the input spectrum:

$$\varepsilon(p_T) = \frac{dN_\eta/dp_T|_{output}}{dN_\eta/dp_T|_{input}} \ . \tag{4.8}$$

The efficiency depends on detector effects as well as on the input spectrum, so an input spectrum $dN/d_T|_{input}$ is used as start spectrum of the efficiency calculation. The simulation then takes into account detector effects affecting the input spectrum and releases an output spectrum $dN/d_T|_{output}$. To optimize the calculation, an iterative procedure is used, in which the corrected output spectrum is used as the input spectrum of the next iteration. The reconstruction efficiency is finally calculated by dividing the output spectrum, given by the result of the simulation, by the input spectrum which is given by the input parameters of the simulation. The efficiency is not limited to $\varepsilon < 1$ due to equation 4.8. An example for the efficiency is shown in Figure 4.5.
To simulate detector effects, the energies and the hit positions of the decay photons have to be smeared. The energy smearing has a constant and an energy dependent term and follows the functional form

$$\sigma_E/E = \frac{A}{\sqrt{E/GeV}} \oplus B \ . \tag{4.9}$$

The parameters for equation 4.9 are given in Table 4.3.4 for the different collision systems and the two detector types of the EMCal. The initial values have been taken from former π^0 analyses. The efficiency correction also takes into account the different cuts used for particle identification. The simulation must consider the loss

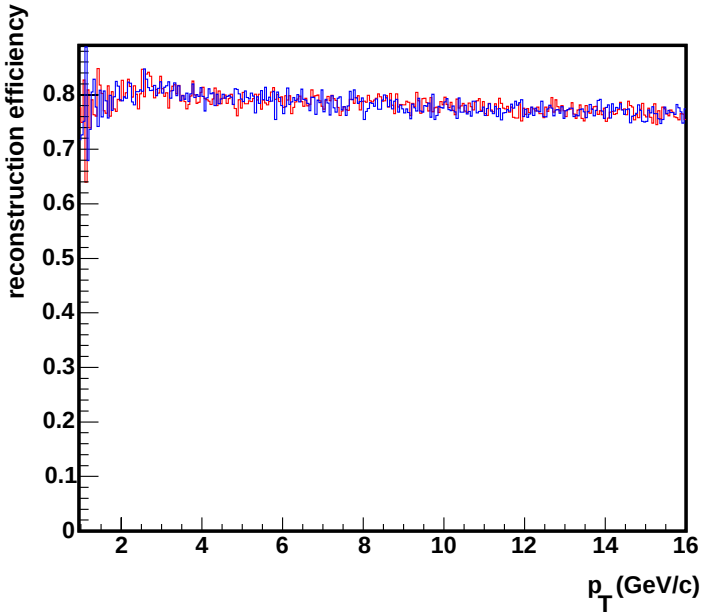

Figure 4.5: Reconstruction efficiency for the η meson in both d+Au (red) and p+p (blue) collisions at PHENIX in Run 3 with an asymmetry cut $\alpha < 0.7$ for PID 3.

collision system	detector type	energy dependent term (A)	constant term (B)
p+p	PbGl	0.085	0.059
	PbSc	0.082	0.050
d+Au	PbGl	0.085	0.067
	PbSc	0.082	0.050

Table 4.1: Parameters for energy smearing as used in the fastMC for the different detector types and the different collision systems.

of photons and thus of η's due to the dispersion and the energy cut. The dispersion cut is estimated by a comparison of uncorrected π^0 spectra [1] without a PID cut with the spectra with the different PID cuts. The spectra are obtained with a sharp asymmetry cut and as a function of $(E_1 + E_2)/2$. This loss of neutral pions is translated into a photon loss probability, which is then used in the simulation:

$$p^{\gamma}_{survival} = \sqrt{p^{\pi^0}_{survival}} \; . \tag{4.10}$$

The energy cut is reproduced by rejecting photon hits according to an energy dependent survival probability in the simulation.
Finally, the simulation reconstructs the invariant mass and the transverse momentum of the η's from the smeared information. Only particles inside the interval used for the integration of the real peak are accepted. As a check, the position and the width of the simulated peak are compared to the position and the width of the measured peak. The simulated peak should not differ much from the measured peak. The comparison is shown in Figure 4.6. In general, there is a good agreement, but as the smearing parameters are adjusted with help of the π^0 peak, the comparison of the simulated and the measured width of the η peak in d+Au collisions shows some deviation. As this deviation does not have any significant effect on the fully corrected η spectra, the possible small deviation in yield is considered in the systematic errors (see 4.3.5).

Bin-shift Correction

The bin-shift correction takes into account that the data points of the η spectra are plotted at the center of a given interval. Due to the exponentially falling spectrum this does not represent the true physical value. So a correction has to be applied; either the data points are moved horizontally keeping their y-value or the points are moved vertically keeping their p_T-values.
The second method is preferable because the different spectra will keep their x-values and can thus be compared much better by taking point-to-point ratios. First a function $f(p_T)$ is used to parameterize the η spectrum. This function is regarded to be a good approximation to the "true" spectrum. Now the value r, the ratio of

[1] Here, the spectra of π^0's are used due to much better statistics. The π^0 spectra are extracted from the invariant mass spectra as described in [Kle03].

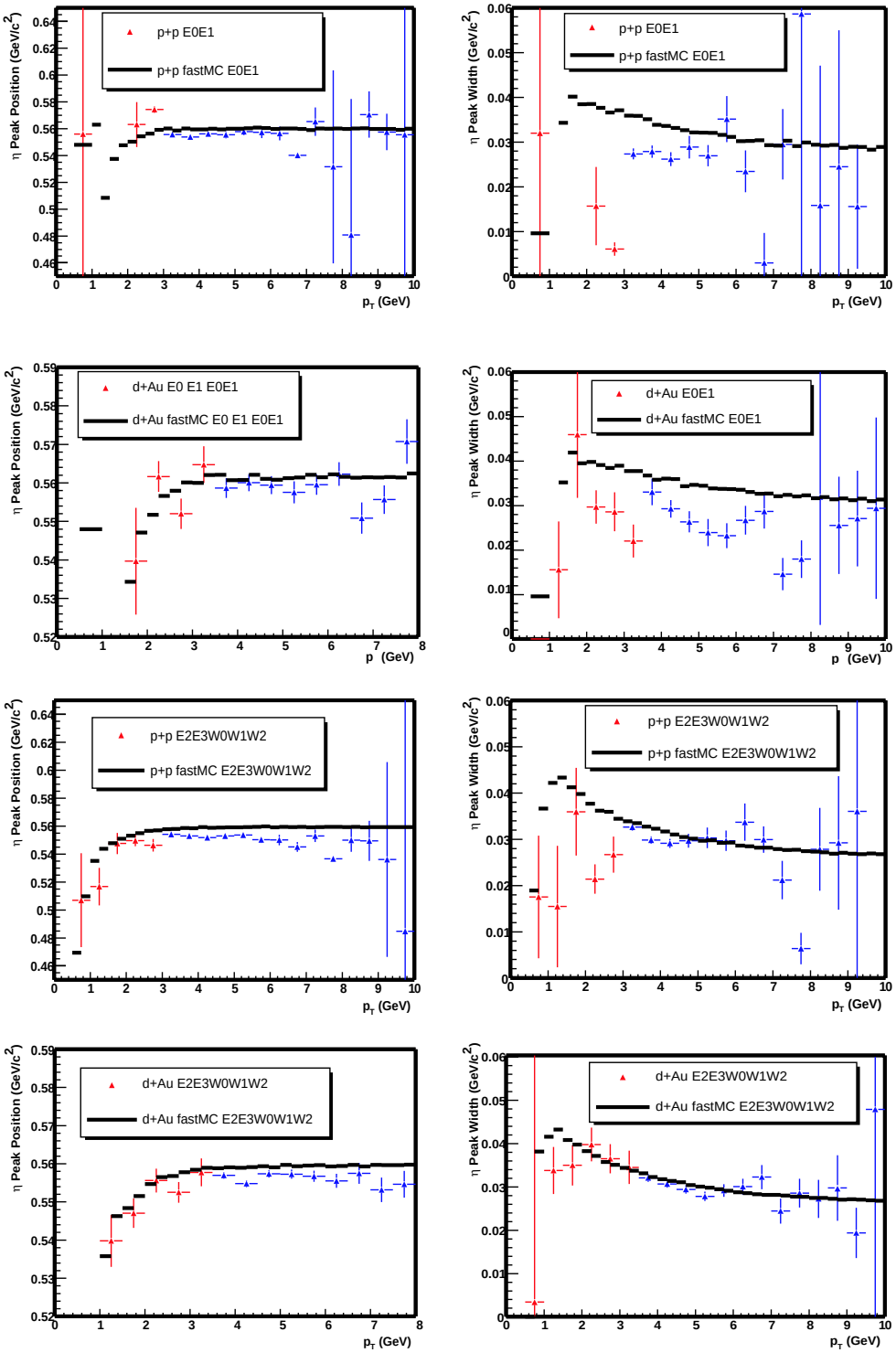

Figure 4.6: Comparison of the simulated peak positions (left) and the simulated peak widths (right) to the measured data for the two different detector types for minimum bias d+Au and p+p collisions. The red points are minimum bias events, the blue points are high p_T triggered events.

collision system	correction due to minimum bias trigger efficiency
p+p min bias	0.659
d+Au 0-20 central	1.0
d+Au 20-40 semicentral	0.995
d+Au 40-60 semiperipheral	0.974
d+Au 60-88 peripheral	0.885

Table 4.2: Correction factors due to the efficiency of the minimum bias trigger for different types of collisions. [Dre03]

the average value of the function inside the p_T interval with a given width Δ and of the value of the function f at the bin center, p_T^c, is calculated:

$$r = \frac{1/\Delta \cdot \int_{p_T^c-\Delta/2}^{p_T^c+\Delta/2} f(p_T)dp_T}{f(p_T^c)} \ . \tag{4.11}$$

The corrected yield Y_{corr} is

$$Y_{corr} = \frac{Y_{uncorr}}{r} \tag{4.12}$$

where Y_{uncorr} denotes the uncorrected yield.

Other Corrections

Minimum Bias Trigger Efficiency The minimum bias trigger does not detect every collision, only a certain fraction ε_{trig} of the inelastic collisions and a fraction ε_η of the η mesons can be observed. For example, $\varepsilon_{trig} = 0.517$ and $\varepsilon_\eta = 0.785$ for p+p collisions. The spectra have to be corrected for both of these effects. The correction factors $\frac{\varepsilon_{trig}}{\varepsilon_\eta}$ are shown in Table 4.3.4.

ERT Trigger Efficiency The efficiency of the ERT trigger has to be studied as well to get η spectra for the ERT triggered data at high transverse momenta. This efficiency has been determined for previous π^0 analyses [Aph03b] where it has principally been determined by calculating the ratio of the number of π^0's in minimum bias events that carry the ERT flag to the number of π^0's in all minimum bias events. An example of the ERT trigger efficiency is given in Figure 4.7.

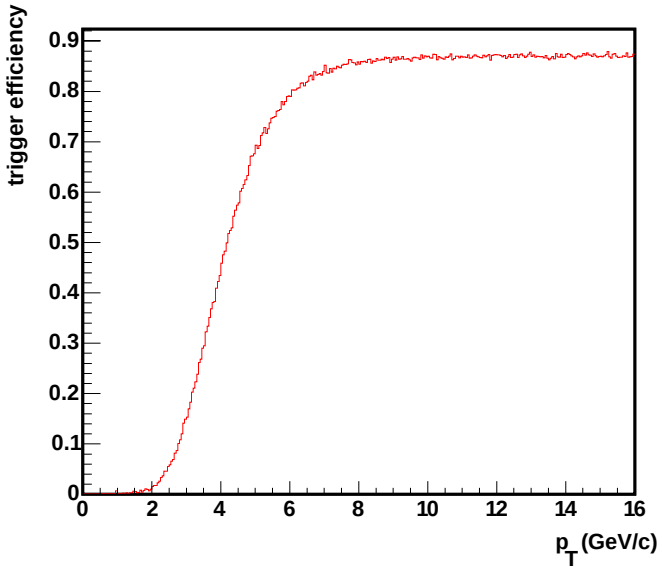

Figure 4.7: Simulation result for the efficiency of the ERT trigger in d+Au collisions.

$\eta \rightarrow 2\gamma$ Branching Ratio The branching ratio of the measured decay of the eta meson is (0.3943 $\pm$ 0.0026) (see section 4.1). The spectrum is thus divided by this value to take this branching ratio into account.

Photon Conversion Some η's are not measured due to conversion of the decay photons in the inner regions of the PHENIX detector. The correction factor takes into account that some η's are measured although one or both decay photons convert, the correction factor is 1.0685 $\pm$ 0.036 (see [Kle03]).

4.3.5 Error Estimation

Each analysis step leads to errors which have to be calculated or estimated. A statistical error results from the peak extraction, systematic errors are made in the peak extraction as well as in the different corrections applied to the raw spectrum.

Statistical Error

The considerations about the statistical error are basically the same as described in [Awe01]. They are based on the following argument:
The measured number of η mesons per p_T-interval in the real event distribution

(N) is considered to be the sum of the number of correlated pairs (S) and the uncorrelated pairs (B)

$$N = S + B \ . \tag{4.13}$$

The background B is unknown, it is estimated from the mixed-events distribution M with

$$B' = kM \tag{4.14}$$

with k denoting the background scale parameterization. The expected value $\langle B' \rangle$ is the same as the expectation value of the background $\langle B \rangle$. With 4.14, the number of the measured η's and respectively the number of correlated pairs S can be estimated as

$$S' = N - B' = N - kM \ . \tag{4.15}$$

Here again, $\langle S' \rangle = \langle S \rangle$. These assumptions lead to the statistical error of the number of correlated pairs, supposing that the error of the fit $\epsilon^2(k)$ is dominated by the error in the constant parameter:

$$\begin{aligned} \epsilon^2(S') &= \epsilon^2(N) + \epsilon^2(k)M^2 + k^2\epsilon^2(M) && (4.16)\\ &= N + \epsilon^2(k)M^2 + k^2 M && (4.17)\\ &= S' + B' + \epsilon^2(k)M^2 + k^2 M && (4.18) \end{aligned}$$

Systematic Errors

There are various sources of systematic errors, they can be classified in three different categories.

Type A errors are probably correlated to the transverse momentum, but as the possible correlation is not known, these errors are treated as p_T-uncorrelated,

Type B errors are p_T-correlated and move all points to the same direction by different factors,

Type C errors are p_T-correlated as well and move all points to the same direction by the same factor.

All systematic errors are estimated with 1σ uncertainty. An overview of the errors is given in Table 4.3.

	p_T indep.	2 GeV	6 GeV	10 GeV	type
peak extraction	8.0 %				A
geometric acceptance		3.0 %	2.0 %	2.0 %	B
η reconstruction efficiency		4.0 %	4.0 %	4.5 %	B
Trigger efficiency		-	5.0 %	3.0 %	B
energy scale		1.0 %	7.0 %	7.5 %	B
Trigger Normalization Scale	5.0 %				C
Conversion correction	2.8 %				C
Total error		11 %	16 %	16 %	

Table 4.3: Systematic errors of the η invariant yields.

Peak Extraction Systematic errors in the peak extraction occur due to the background parameterization with a certain functional form. The error is estimated by using different functional forms, here by fitting the background with a linear function instead of a second degree polynomial. Overall it can be estimated to be 8 %.

Geometric Acceptance Although the geometry of the detector is very well known, the parameterization of the difference between the impact point of the photon on the detector surface and the maximum tower position of a cluster leads to some uncertainty in the fastMC. This uncertainty was estimated in a previous analysis of neutral pions (see [Rey03]).

Reconstruction Efficiency The reconstruction efficiency calculation has to regard the cuts for photon identification as well as the resolution smearing of the detectors. Thus there are two sources leading to systematic errors in the reconstruction efficiency. The error due to the PID cuts is estimated by comparing the fully corrected yields for the different PID classes, an example is given in Figure 4.8. Changing the energy smearing in the fastMC results in an estimation of the error due to this uncertainty. The quadratic sum of these two errors is given in Table 4.3.

Trigger Efficiency As the trigger efficiency used for the analysis of η mesons is taken from an earlier analysis, the error which has been taken from the trigger efficiency studies in this analysis [Aph03b] should be the same in the η analysis.

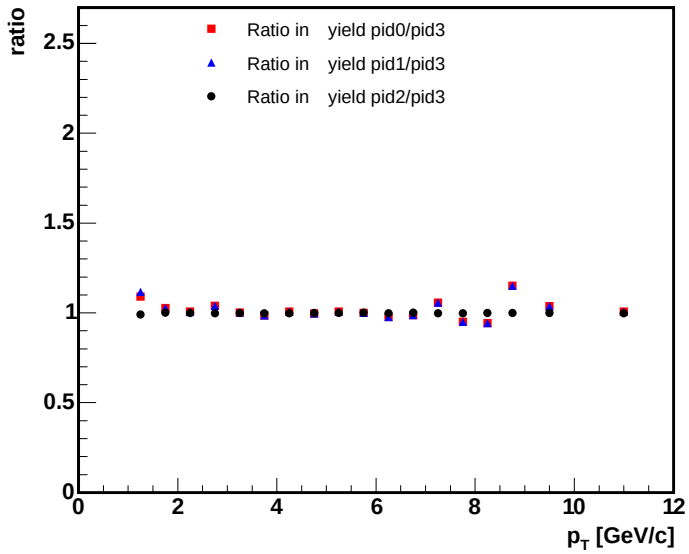

Figure 4.8: Ratio in yield with PID 2 and PID 3 for d+Au as a function of p_T.

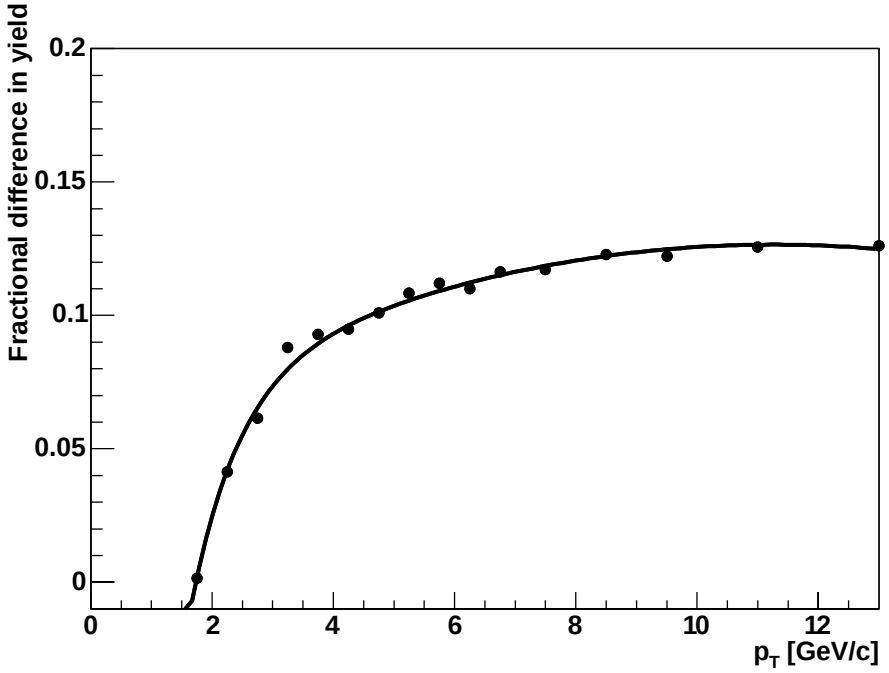

Figure 4.9: Error in yield due to the uncertainty in energy scale for d+Au as a function of p_T.

Energy Scale The peak positions obtained by a Gaussian fit of the invariant mass spectra in the peak region have to be reproduced by the fastMC. Here, the energy shifts reproducing the peak positions vary by about 2 %, so the 1 σ uncertainty can be estimated at about 1.5 %. This uncertainty leads to an error in the η yield which

is estimated by varying the energy scale in the fastMC by 1.5 %. The fractional difference of the yields as shown in Figure 4.9 gives the respective error in yield.

Trigger Normalization Scale Two different methods for obtaining the normalization of the ERT trigger have been used in [Rey03] and in [Aph03b]. The comparison of the scale factor of the two methods leads to a difference of about 5 %. Because the two methods both give reasonable estimates of the normalization scale, they are expected to be within 1 σ.

Conversion Correction The estimation of the conversion correction in [Rey03] used for the η analysis contains a 2.8 % error.

5 Results of the η Measurement

The first important result are p_T spectra of η mesons for the different reaction systems. These invariant yields are used to calculate the nuclear modification factor R_{AB} to study possible nuclear medium effects and to calculate the ratio of η and π^0 which should follow the m_T scaling.

5.1 η Spectra

The fully corrected invariant yield of the η meson is shown in Figure 5.1 for minimum bias events in proton-proton and in deuterium-gold collisions at $\sqrt{s_{NN}} = 200$ GeV. The error bars represent the total error, the quadratic sum of the statistical

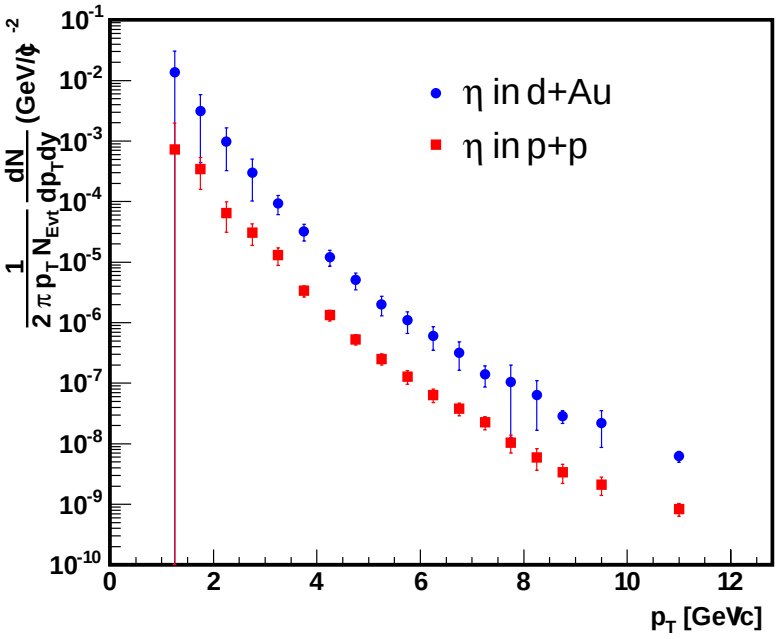

Figure 5.1: The p_T spectra of the η invariant yields in minimum bias p+p and d+Au events at $\sqrt{s_{NN}} = 200$ GeV. The invariant yield is calculated by dividing the invariant cross section by the total inelastic cross section which is taken as $\sigma_{NN} = 42.2$ mb in $\sqrt{s_{NN}} = 200$ GeV at PHENIX.

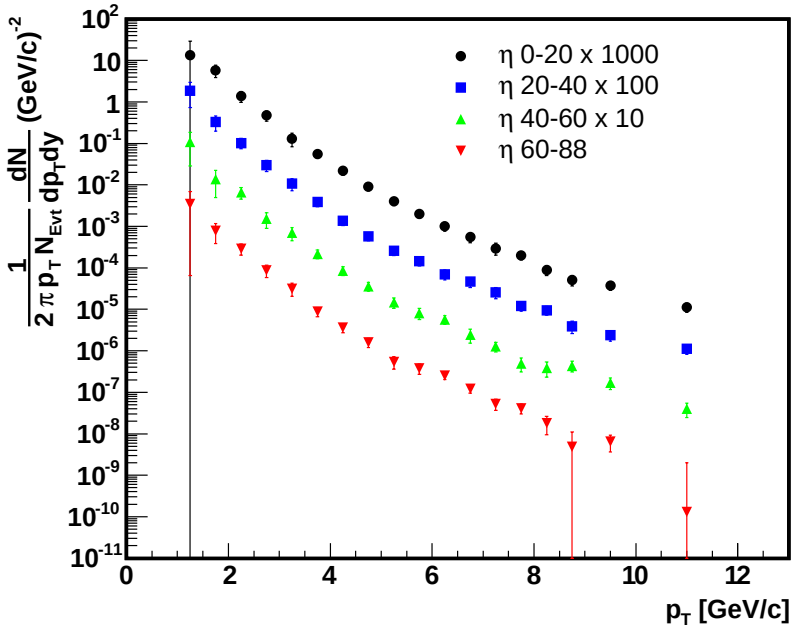

Figure 5.2: The p_T spectra of the η invariant yields in d+Au events with four different centralities at $\sqrt{s_{NN}}$ = 200 GeV.

and the systematic errors.

Figure 5.1 shows the η invariant yields for four different centrality classes in d+Au collisions at $\sqrt{s_{NN}}$ = 200 GeV. The error bars represent the quadratic sum of the statistical and the systematic errors.

5.2 Nuclear Modification Factor

The measurements of the η meson aim at studying possible nuclear medium effects in d+Au collisions in general and their dependence on the centrality of the collisions. Therefore the nuclear modification factor (see equation 2.5) is calculated for minimum bias and for centrality dependent spectra in d+Au collisions using the spectrum in p+p collisions as baseline. The number of collisions N_{coll} is calculated in a Glauber calculation [Dre03]. The main idea in Glauber calculations is a geometrical model assuming straight nucleon trajectories and constant cross sections

centrality bin	N_{coll}
0-20	15.0 ± 1.0
20-40	10.4 ± 0.7
40-60	6.9 ± 0.6
60-88	3.2 ± 0.3

Table 5.1: Values of N_{coll} for the different centralities in d+Au collisions. [Dre03]

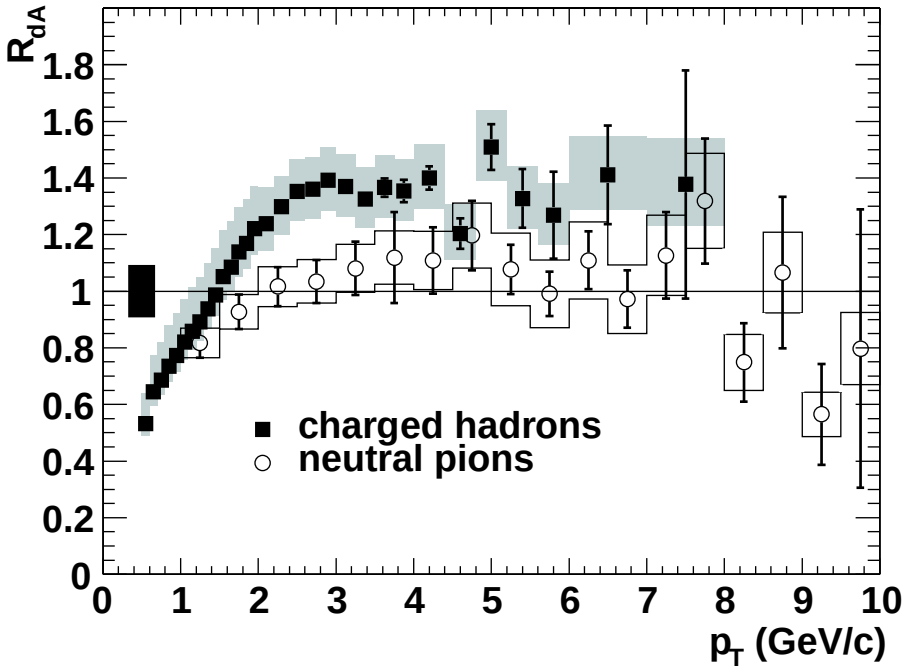

Figure 5.3: Nuclear modification factor R_{dA} for neutral pions and charged hadrons in $\sqrt{s_{NN}} = 200$ GeV d+Au collisions. [Adl03b]

between the nucleons before and after an interaction. The results are given in Table 5.1.

The nuclear modification factor for d+Au collisions is called R_{dA}, it has been measured for neutral pions and charged hadrons as published in [Adl03b], the main result is shown in Figure 5.3. One important information given by this measurement is the absence of a suppression of particles with high transverse momenta in d+Au collisions and the observation of a Cronin enhancement in the particle production, especially for charged hadrons.

5.2.1 Systematic Errors of R_{dA}

The systematic errors in the d+Au and the p+p analysis result from the same sources as described in Section 4.3.5. Some of these errors will cancel out when calculating the nuclear modification factor. The error due to the η reconstruction efficiency as well as the error due to uncertainties in the energy scale occur when applying detector effects to the measured data. These detector effects are very similar for the measurement of η mesons in p+p and d+Au collisions as the measured data have been taken in the same experimental run.
Otherwise the active detector surface that is important for the acceptance determination is different in the two analyses because different modules have been found to be bad. Thus the systematic error in acceptance will not cancel. The errors due to the high p_T trigger do not cancel as well as two different thresholds of the ERT have been used for the d+Au and the p+p analysis.

5.2.2 Results of R_{dA} for η Mesons

The nuclear modification factor of η mesons for minimum bias $\sqrt{s_{NN}} = 200$ GeV d+Au collisions is shown in Figure 5.4. The data points at lower transverse momenta have large statistical errors. This is caused by the bad signal to background ratio of the η peak in the sample that is not triggered with the ERT.
The result shows that there is no suppression of η mesons at high transverse momenta in d+Au collisions. For $p_T > 3$ GeV/c the results are consistent with a slight enhancement caused by the Cronin effect as observed for neutral pions and charged hadrons in $\sqrt{s_{NN}} = 200$ GeV collisions [Adl03b].

The results for the nuclear modification factor of η's for different centralities in $\sqrt{s_{NN}} = 200$ GeV collisions are shown in Figure 5.5. The most important observation is a possible centrality dependence of R_{dA} as observed for neutral pions. In peripheral collisions, the π^0 R_{dA} shows a light suppression while there is an enhancement in central collisions. The η data are consistent with that observation within the errors. This suggests that the Cronin enhancement which is caused by multiple soft scattering does not occur in peripheral d+Au collisions.

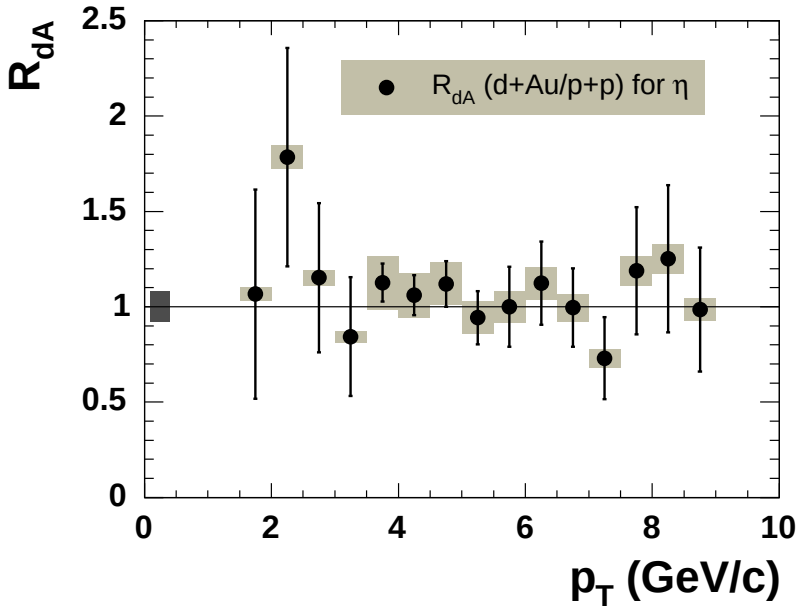

Figure 5.4: The nuclear modification factor R_{dA} for η mesons as a function of p_T for $\sqrt{s_{NN}} = 200$ GeV d+Au collisions.

5.3 Ratio of η and π^0

Figure 5.6 shows the invariant yields for η and π^0 in minimum bias d+Au collisions as a function of the transverse mass $m_T = \sqrt{p_T^2 + m_0^2}$. The spectrum keeps its shape for particles with different masses as η and π^0 due to m_T scaling.
The m_T spectra of η and π^0 are shown in Figure 5.6. As the spectra of the two particles are parallel inside the errors as predicted by m_T scaling, the first step to determine the ratio of η and π^0 is the parameterization of the π^0 spectrum with a fit following equation 2.2.

$$E\frac{d^3N}{dm_T^3} = c \cdot \left(\frac{p_0}{m_T + p_0 \cdot e^{-am_T}}\right)^n . \tag{5.1}$$

The results for the fit parameters p_0, a and n are shown in Table 5.2. These parameters are fixed in the next step, only the parameter c is free in the fit to the η spectrum. The ratio $R = c_\eta / c_{\pi^0}$ denotes the production ratio of the two particles.
The parallel progression of the invariant yields in m_T leads to a p_T dependence of the production ratio of the two mesons due to the larger mass of the η. This ratio

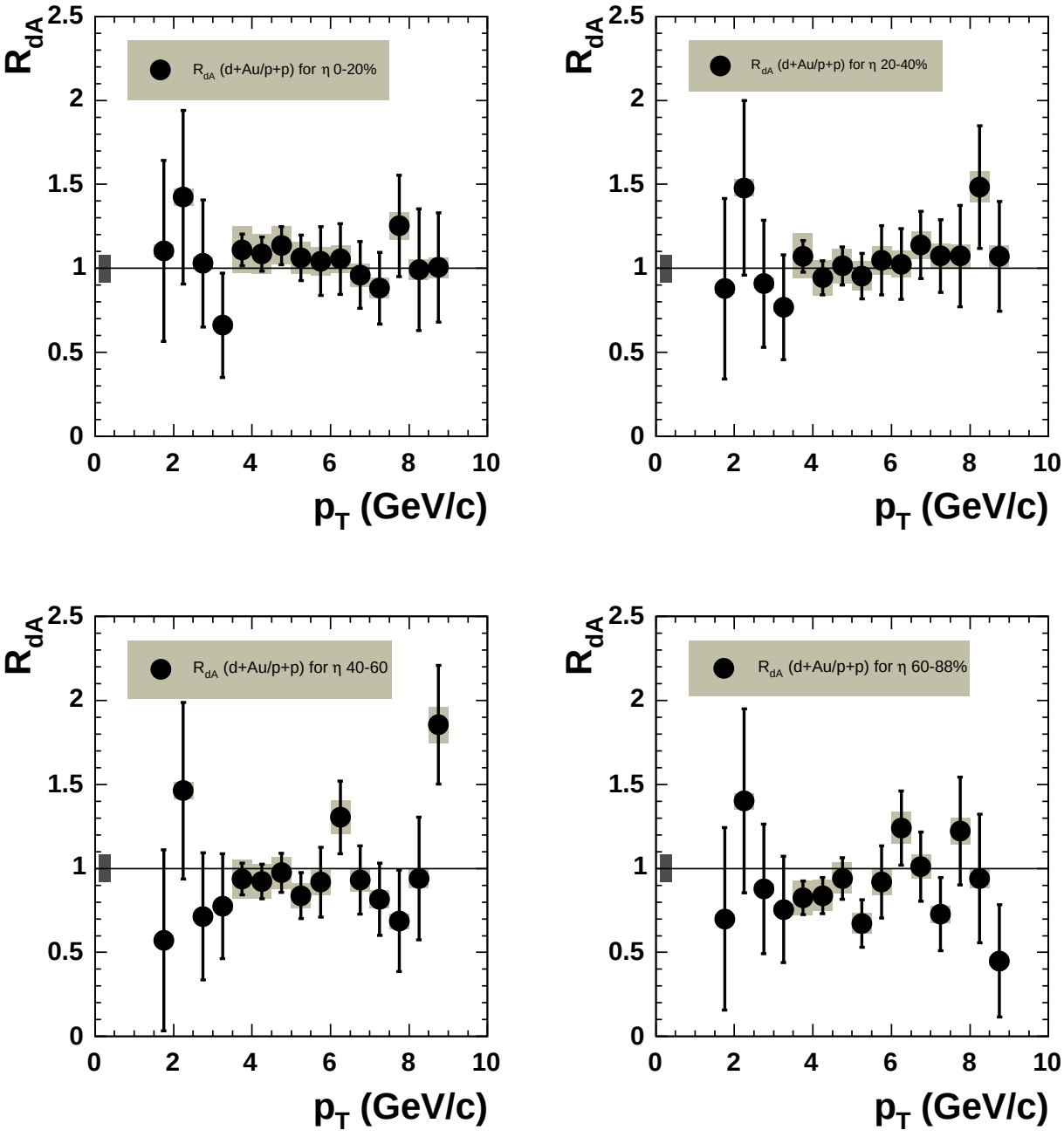

Figure 5.5: The nuclear modification factor R_{dA} as a function of p_T for $\sqrt{s_{NN}} = 200$ GeV d+Au collisions in four different centrality classes.

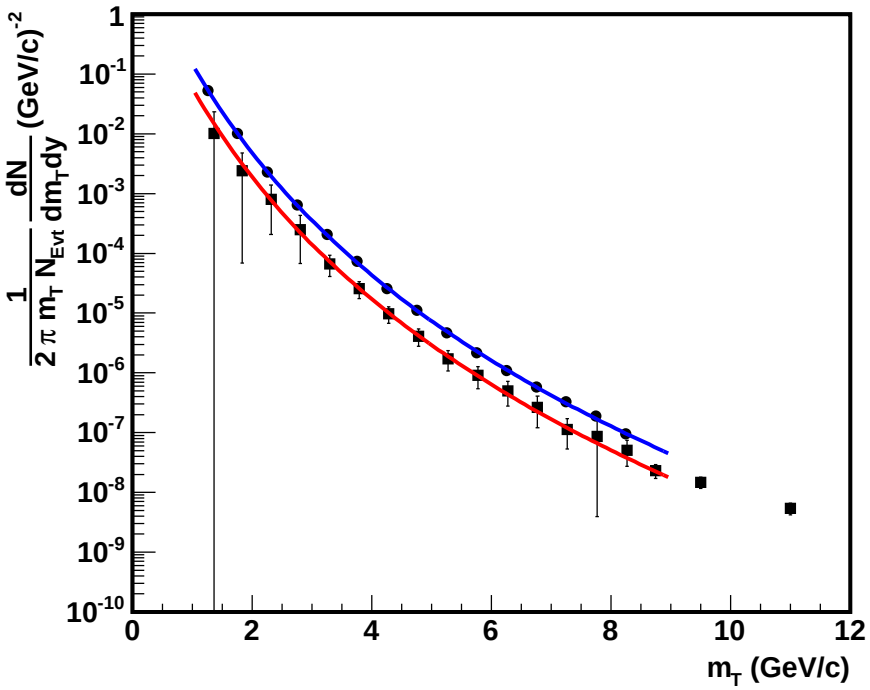

Figure 5.6: The m_T spectra of η and of π^0 in minimum bias $\sqrt{s_{NN}} = 200$ GeV d+Au collisions. The fit functions parameterize the spectra with Function 5.1, the fit parameters describing the form of the function are the same, only the constant term is different. The π^0 spectrum is taken from [Adl03b].

analysis class	Fit parameters p_0	a	n
d+Au minimum bias	1.774	$6.451 \cdot 10^{-10}$	11.06
d+Au 0-20 central	1.729	$7.905 \cdot 10^{-9}$	11.08
d+Au 20-40 semicentral	1.023	0.441	8.701
d+Au 40-60 semiperipheral	1.004	0.446	8.671
d+Au 60-88 peripheral	1.280	$1.575 \cdot 10^{-8}$	10.03
p+p minimum bias	1.320	$5.329 \cdot 10^{-9}$	10.28

Table 5.2: The parameters of function 5.1 when used for the parameterization of the η yields for the four centrality classes in $\sqrt{s_{NN}} = 200$ GeV d+Au collisions and for minimum bias $\sqrt{s_{NN}} = 200$ GeV d+Au and p+p collisions.

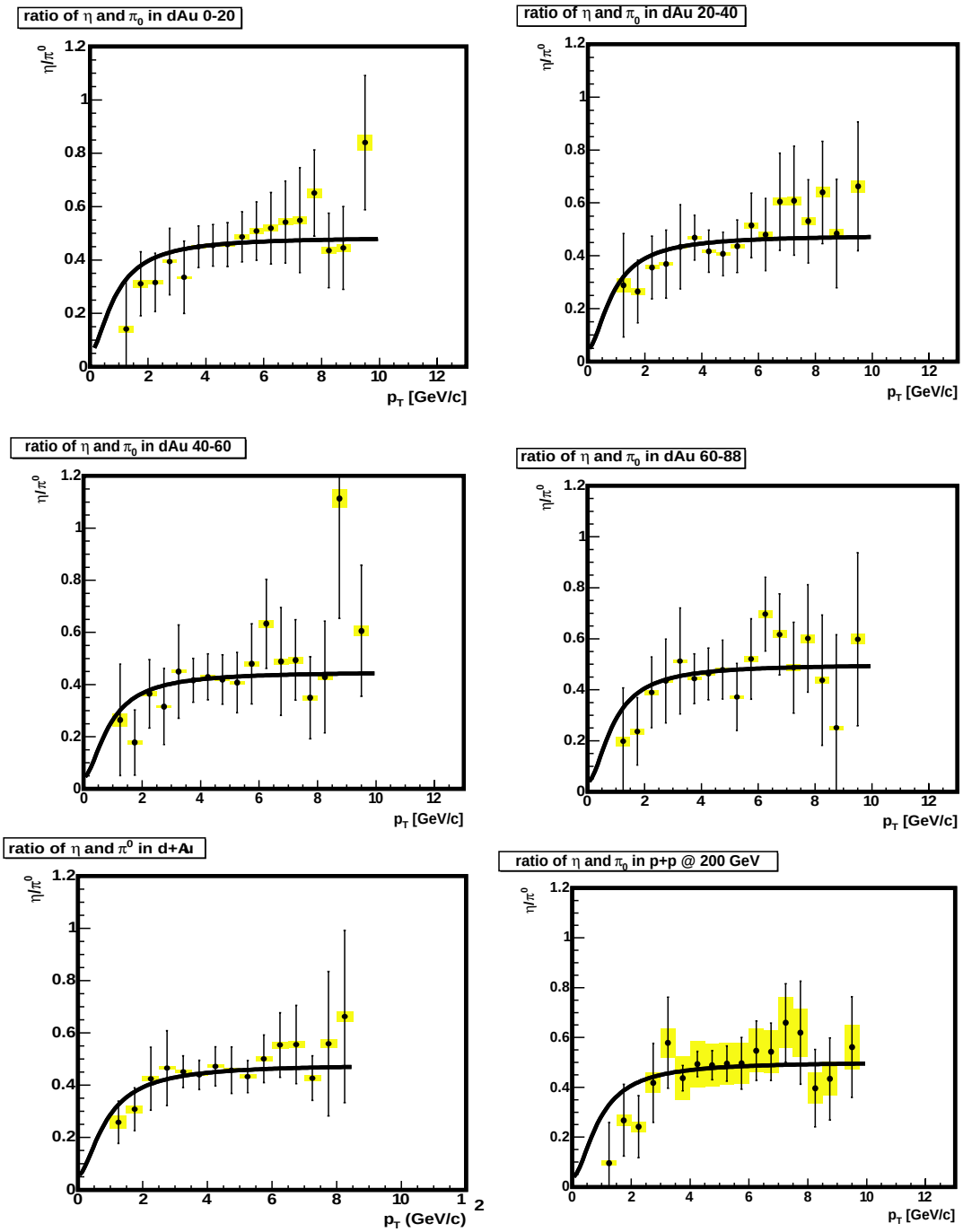

Figure 5.7: The ratio η/π^0 for the different collision systems and centrality classes. The error bars represent the statistical errors, the boxes represent the systematic errors.

is shown in Figure 5.7 for the different measured systems. The data points are parameterized with a function resulting from the conversion from m_T to p_T, assuming m_T scaling. This parameterization function results from equation 5.1:

$$\frac{E\frac{d^3N}{dp_T^3}(\eta)}{E\frac{d^3N}{dp_T^3}(\pi^0)} = R \cdot \left(\frac{p_0 e^{-a\sqrt{m_{\pi^0}^2+p_T^2}} + \sqrt{m_{\pi^0}^2+p_T^2}}{p_0 e^{-a\sqrt{m_\eta^2+p_T^2}} + \sqrt{m_\eta^2+p_T^2}} \right)^n . \tag{5.2}$$

For the parameterization shown in Figure 5.7, the parameters p_0, a and n are fixed to the values shown in Table 5.2. The only free parameter is R. The results for R are shown in Table 5.3.
The ratio of η and π^0 has been determined in previous measurements. A compilation of these data can be found in [dEn04], the data points are shown in Figure 5.3. A linear fit to these data points in the region above $p_T \approx 1.5$ GeV gives an η/π^0 ratio of about 0.45 according to [dEn04]. A fit of all these data points with the functional form 5.2 leads to a η/π^0 ratio of $R \approx 0.483 \pm 0.006$.
The ratio of η and π^0 is calculated with published π^0 spectra measured at PHENIX for p+p [Adl03c] and minimum bias d+Au [Adl03b] collisions. As neutral pion baseline for the different centralities in d+Au, results from the analysis described in [Bat03] are used. The results of that analysis are to be published in the near future. As the analyses leading to the spectra of neutral pions and of η's is very similar and uses the same methods, the systematic errors in d+Au collisions cancel with one exception when the ratio η/π^0 is calculated. The error due to the uncertainty in the energy scale of the EMCal is smaller for the η (see 4.3.5), so this error does not cancel completely. Another exception is the p+p case because the spectra for π^0's and η's are from different experimental runs.

Within the errors, the η/π^0 ratio measured by PHENIX is consistent with the collected data from former measurements. There are no significant changes in the η/π^0 ratio for different centralities in d+Au collisions or for minimum bias d+Au and p+p collisions.

analysis class	Fit parameter R
d+Au minimum bias	0.479 ± 0.025
d+Au 0-20 central	0.485 ± 0.031
d+Au 20-40 semicentral	0.477 ± 0.033
d+Au 40-60 semiperipheral	0.449 ± 0.036
d+Au 60-88 peripheral	0.499 ± 0.040
p+p minimum bias	0.502 ± 0.025

Table 5.3: The parameter R of function 5.2 when used for the parameterization of the ratio of η and π^0 for the four centrality classes in $\sqrt{s_{NN}} = 200$ GeV d+Au collisions and for minimum bias $\sqrt{s_{NN}} = 200$ GeV d+Au and p+p collisions.

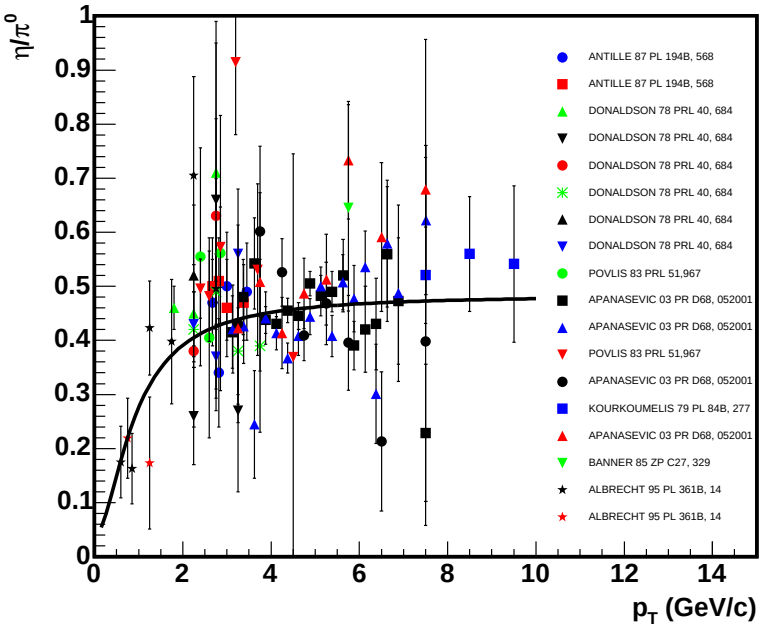

Figure 5.8: World data of the ratio η/π^0.

6 Conclusion

In this thesis, the production of η mesons in p+p and d+Au collisions at collision energies of $\sqrt{s_{NN}} = 200$ GeV has been studied. The analysis of both reactions is based on measurements of the PHENIX experiment at the RHIC collider at BNL. The results of the measurements have been used to calculate the nuclear modification factor R_{dA} and the production ratio of the η and the π^0 meson.

The transverse momentum distribution of the η meson can be reconstructed via its two photon decay. The photons are measured with the PHENIX detector, the thesis describes the steps which are necessary to obtain fully corrected transverse momentum distributions for the different collision systems.

The nuclear modification factor is calculated as the ratio of the η production yields in d+Au and p+p collisions scaled by the number of binary nucleon-nucleon collisions N_{coll}. It is used to quantify possible nuclear medium effects in nucleon-nucleus and in nucleus-nucleus collisions. The particle yields are expected to scale with N_{coll} for $p_T \gtrsim 2$ GeV/c in absence of such nuclear medium effects.

The results on the nuclear modification factor are similar to the results for neutral pions. In minimum bias d+Au collisions, η mesons are not suppressed. The results are consistent with a light Cronin enhancement of the η production. An expectation from π^0 results is the absence of the Cronin enhancement in peripheral collisions and a centrality dependent increase of this enhancement towards more central collisions. The η results are consistent with this expectation, but due to the errors there is no evidence for this.

Another analysis [dEn03] is going on for the η production in Au+Au collisions at $\sqrt{s_{NN}} = 200$ GeV. Preliminary results indicate a clear suppression of the η meson in central gold collisions. A possible theoretical model for explaining such a suppression is the formation of a Color Glass Condensate (CGC). This initial state effect would lead to a suppression of the η production in central d+Au collisions as well. So the

results presented in this thesis show that the CGC or other initial state effects of the Au nucleus are not responsible for the suppression of η production in central Au+Au collisions.

The η shows a similar behavior to the neutral pion in all collision systems that have been studied at the PHENIX experiment. There is no evidence for a possible mass dependence of the nuclear modification factor in d+Au and Au+Au collisions.

The production ratio of η and π^0 is consistent with the existing "world data". The η spectra were found to follow m_T scaling with respect to the π^0 spectra in d+Au and p+p collisions.

A Kinematic Variables

Ultrarelativistic reactions are described by different kinematic variables to simplify changing the frame of reference (see [Bus02]).
In high energy physics particles are described with the help of the four momentum

$$p^\mu = (E, \vec{p}) = (E, p_x, p_y, p_z) \ . \tag{A.1}$$

Here, E is the energy of a particle while $\vec{p}$ denotes its momentum in cartesic coordinates. In this notation, the variables c and $\hbar$ are set to $c \equiv \hbar \equiv 1$. Free particles with a rest mass m_0 follow the relativistic energy momentum relation

$$E^2 = m_0^2 + \vec{p}^2 \ . \tag{A.2}$$

The norm of the four momentum p^μ, the invariant mass

$$m_{inv}^2 = p^\mu p_\mu = -\vec{p} \cdot \vec{p} + E^2 \tag{A.3}$$

is Lorentz invariant. The Mandelstam variable s, the squared sum of the momenta of the two scattering particles

$$s = (p_1^\mu + p_2^\mu)^2 \ , \tag{A.4}$$

is used to denote the energy of a collision in its center of mass system. The overall collision energy is given by $\sqrt{s}$.
The z axis of the coordinate system in accelerator experiments is determined by the beam axis. So the three momentum of a particle can be split into two components, the longitudinal momentum p_L and the transverse momentum p_T:

$$p_L = p \cdot \cos\vartheta = p_z \tag{A.5}$$

$$p_T = p \cdot \sin\vartheta = \sqrt{p_x^2 + p_y^2}. \tag{A.6}$$

ϑ denotes the angle of the propagation direction of the particle towards the beam axis, $p = |\vec{p}|$ is the norm of the three momentum. Unlike the transverse momentum

p_T, the longitudinal momentum p_L is not Lorentz invariant. Thus the longitudinal velocity $\beta_L = p_L/E$ of particles is described by the rapidity y:

$$y = \operatorname{atanh}(\beta_L) \tag{A.7}$$

$$= \frac{1}{2} \ln \frac{E + p_L}{E - p_L}. \tag{A.8}$$

The rapidity shows an additive behavior when the frame of reference is changed to a system moving with the relative velocity β with respect to the first system

$$y' = y + \operatorname{atanh}(\beta), \tag{A.9}$$

so the shape of the rapidity distribution of a particle is not affected by a change of the frame of reference. The following equations hold:

$$E = m_T \cdot \cosh(y) \tag{A.10}$$

$$p_L = m_T \cdot \sinh(y) \ . \tag{A.11}$$

Here $m_T = \sqrt{p_T^2 + m_0^2}$ denotes the so-called transverse mass of a particle.
If $E \gg m_0$, the rapidity can be approximated by the pseudorapidity η:

$$\eta = \frac{1}{2} \ln \frac{p + p_L}{p - p_L} \tag{A.12}$$

$$= -\ln \left[\tan \left(\frac{\vartheta}{2} \right) \right] \ . \tag{A.13}$$

The pseudorapidity of a particle can be determined with the emission angular to the beam axis ϑ, thus the pseudorapidity is easier to determine in experiments. According to (A.10) and (A.11) it is:

$$p = p_T \cdot \cosh(\eta) \tag{A.14}$$

$$p_L = p_T \cdot \sinh(\eta) \ . \tag{A.15}$$

B Lorentz Invariant Cross Section

The Lorentz invariant cross section $Ed^3\sigma/dp^3$ is often used to describe the particle production in ultrarelativistic reactions (see [Rey99]). The following relations are valid:

$$\begin{aligned} \sigma_{inv} \equiv E\,\frac{d^3\sigma}{d\vec{p}^3} &= E\,\frac{1}{p_T}\,\frac{d^3\sigma}{dp_T\,d\varphi\,dp_L} \\ &\overset{\frac{dp_L}{dy}=E}{=} \frac{1}{p_T}\,\frac{d^3\sigma}{dp_T\,d\varphi\,dy} \\ &\overset{\varphi\text{-symmetry}}{=} \frac{1}{2\pi\,p_T}\,\frac{d^2\sigma}{dp_T\,dy} \qquad \text{(B.1)} \\ &= \frac{1}{2\pi\,m_T}\,\frac{d^2\sigma}{dm_T\,dy}\ . \qquad \text{(B.2)} \end{aligned}$$

Looking at one special particle species Y produced in inelastic reactions, the integration of the Lorentz invariant cross section leads to the product of the average number of particles produced in each inelastic reaction and the total inelastic cross section:

$$\int E\,\frac{d^3\sigma}{d\vec{p}^3}\,d\vec{p}^3 = \langle n_Y\rangle \cdot \sigma_{in}\ . \qquad \text{(B.3)}$$

The Lorentz invariant cross section is determined experimentally as

$$E\,\frac{d^3\sigma}{d\vec{p}^3} = \frac{1}{2\pi\,p_T\,N_{in}} \cdot \frac{\Delta N_Y}{\Delta p_T\,\Delta y} \cdot \sigma_{in}\ . \qquad \text{(B.4)}$$

Here, ΔN_Y is the overall number of particles measured in the transverse momentum interval $[p_T, p_T + \Delta p_T]$ and the rapidity interval $[y, y + \Delta y]$ in N_{in} inelastic reactions.

Sometimes it is easier to measure the yield per event instead of the cross section as it does not depend on the total inelastic cross section. Therefore the Lorentz invariant cross section is divided by the total inelastic cross section σ_{in}:

$$E\,\frac{d^3N}{d\vec{p}^3} = \frac{1}{2\pi\,p_T\,N_{in}} \cdot \frac{\Delta N_Y}{\Delta p_T\,\Delta y}\ . \qquad \text{(B.5)}$$

C Data Tables

p_T	inv. yield	tot. err.	stat. err.	sys. err.	error A	error B	error C
1.25	0.0137796	0.0167189	0.0166405	0.00161758	0.000826774	0.00133572	0.000385828
1.75	0.00314731	0.00270908	0.00269654	0.000260389	0.000188839	0.000156129	8.81247e-05
2.25	0.000983157	0.000659016	0.000653791	8.28195e-05	5.89894e-05	5.12007e-05	2.75284e-05
2.75	0.000302104	0.000200168	0.00019826	2.75708e-05	1.81262e-05	1.89746e-05	8.45891e-06
3.25	9.3469e-05	3.26973e-05	2.52602e-05	2.07613e-05	5.60814e-06	1.92585e-05	5.35635e-06
3.75	3.22094e-05	9.98634e-06	7.56611e-06	6.51774e-06	1.93256e-06	5.94467e-06	1.8458e-06
4.25	1.21043e-05	3.5915e-06	2.79093e-06	2.26044e-06	7.26259e-07	2.02509e-06	6.93653e-07
4.75	5.0605e-06	1.56625e-06	1.29348e-06	8.83201e-07	3.0363e-07	7.77016e-07	2.89998e-07
5.25	2.02191e-06	7.19343e-07	6.37249e-07	3.3372e-07	1.21315e-07	2.88489e-07	1.15868e-07
5.75	1.08861e-06	4.21813e-07	3.85268e-07	1.7174e-07	6.53163e-08	1.4607e-07	6.23838e-08
6.25	6.06818e-07	2.55794e-07	2.38541e-07	9.23514e-08	3.64091e-08	7.74203e-08	3.47744e-08
6.75	3.21382e-07	1.58785e-07	1.51498e-07	4.75496e-08	1.92829e-08	3.93692e-08	1.84172e-08
7.25	1.39715e-07	5.30703e-08	4.90662e-08	2.02229e-08	8.38291e-09	1.65707e-08	8.00655e-09
7.75	1.05682e-07	9.30299e-08	9.18061e-08	1.50403e-08	6.3409e-09	1.22199e-08	6.05621e-09
8.25	6.33265e-08	4.66909e-08	4.58356e-08	8.89637e-09	3.79959e-09	7.17905e-09	3.629e-09
8.75	2.83356e-08	6.70184e-09	5.42032e-09	3.94142e-09	1.70014e-09	3.16348e-09	1.62381e-09
9.5	2.20041e-08	1.33174e-08	1.29686e-08	3.02815e-09	1.32025e-09	2.4159e-09	1.26097e-09
11	6.20529e-09	1.28558e-09	9.70219e-10	8.43439e-10	3.72317e-10	6.6807e-10	3.55601e-10

Table C.1: Data table of the spectrum measured in p+p. The errors reflect the absolute errors. tot. err. reflects the systematic plus statistical error; stat. err. reflects the statistical error; sys. err. reflects the total systematic error; error A reflects the point-to-point systematic error; error B reflects systematic errors that are correlated in p_T but allow the shape of the result to change; error C reflects the normalization error.

p_T	inv. yield	tot. err.	stat. err.	sys. err.	error A	error B	error C
1.25	0.000732465	0.00125946	0.00125665	8.41318e-05	5.12725e-05	6.34718e-05	2.0509e-05
1.75	0.000347284	0.00018755	0.00018494	3.11795e-05	2.43099e-05	1.69303e-05	9.72396e-06
2.25	6.47854e-05	3.36102e-05	3.30826e-05	5.93174e-06	4.53498e-06	3.36586e-06	1.81399e-06
2.75	3.08248e-05	1.18271e-05	1.14384e-05	3.00714e-06	2.15773e-06	1.90845e-06	8.63093e-07
3.25	1.30382e-05	4.16478e-06	3.94489e-06	1.33538e-06	9.12675e-07	9.03877e-07	3.6507e-07
3.75	3.3629e-06	7.19031e-07	2.01542e-07	6.90207e-07	2.35403e-07	6.19542e-07	1.92715e-07
4.25	1.34185e-06	2.72758e-07	9.68689e-08	2.54977e-07	9.39298e-08	2.24226e-07	7.68965e-08
4.75	5.31657e-07	1.05742e-07	4.69369e-08	9.4754e-08	3.7216e-08	8.16396e-08	3.04672e-08
5.25	2.52409e-07	5.16352e-08	2.90294e-08	4.27023e-08	1.76687e-08	3.60843e-08	1.44646e-08
5.75	1.28056e-07	3.22528e-08	2.46628e-08	2.07843e-08	8.96389e-09	1.72564e-08	7.33838e-09
6.25	6.35352e-08	1.60358e-08	1.25492e-08	9.98326e-09	4.44747e-09	8.16266e-09	3.64096e-09
6.75	3.79567e-08	9.12013e-09	7.02416e-09	5.81704e-09	2.65697e-09	4.69545e-09	2.17515e-09
7.25	2.25116e-08	5.66252e-09	4.53932e-09	3.38507e-09	1.57581e-09	2.70394e-09	1.29006e-09
7.75	1.04538e-08	3.42261e-09	3.05174e-09	1.54956e-09	7.31765e-10	1.22751e-09	5.99067e-10
8.25	5.95561e-09	2.28882e-09	2.11564e-09	8.73357e-10	4.16893e-10	6.87366e-10	3.41293e-10
8.75	3.38278e-09	1.18024e-09	1.07277e-09	4.92085e-10	2.36795e-10	3.85352e-10	1.93855e-10
9.5	2.10321e-09	6.94002e-10	6.24194e-10	3.03347e-10	1.47225e-10	2.36258e-10	1.20527e-10
11	8.33484e-10	1.99082e-10	1.59597e-10	1.19006e-10	5.83438e-11	9.20704e-11	4.77638e-11

Table C.2: Data table of the spectrum measured in d+Au minimum bias. The errors reflect the absolute errors. tot. err. reflects the systematic plus statistical error; stat. err. reflects the statistical error; sys. err. reflects the total systematic error; error A reflects the point-to-point systematic error; error B reflects systematic errors that are correlated in p_T but allow the shape of the result to change; error C reflects the normalization error.

p_T	inv. yield	tot. err.	stat. err.	sys. err.	error A	error B	error C
1.25	13.3168	15.7554	0.0156603	0.0017289	0.00106535	0.00130962	0.000372872
1.75	5.75363	1.8636	0.00177331	0.000573053	0.000460291	0.000300946	0.000161102
2.25	1.3836	0.409248	0.000384724	0.000139538	0.000110688	7.56197e-05	3.87407e-05
2.75	0.47583	0.128339	0.000117851	5.08134e-05	3.80664e-05	3.09101e-05	1.33233e-05
3.25	0.129505	0.0463475	4.40444e-05	1.44282e-05	1.03604e-05	9.3641e-06	3.62615e-06
3.75	0.0559677	0.0127627	4.99903e-06	1.17429e-05	4.47742e-06	1.03712e-05	3.2073e-06
4.25	0.0218512	0.0046608	1.89823e-06	4.25673e-06	1.74809e-06	3.67368e-06	1.25221e-06
4.75	0.00905649	0.00188253	8.90717e-07	1.65848e-06	7.24519e-07	1.39867e-06	5.18993e-07
5.25	0.00401931	0.00083613	4.57543e-07	6.99835e-07	3.21545e-07	5.77343e-07	2.30331e-07
5.75	0.00200375	0.000433785	2.75492e-07	3.35073e-07	1.603e-07	2.70911e-07	1.14827e-07
6.25	0.00100665	0.000246132	1.84376e-07	1.63054e-07	8.0532e-08	1.29513e-07	5.76873e-08
6.75	0.000547116	0.000142209	1.12918e-07	8.64462e-08	4.37692e-08	6.76328e-08	3.13531e-08
7.25	0.00029778	9.50351e-05	8.30737e-08	4.61566e-08	2.38224e-08	3.56612e-08	1.70646e-08
7.75	0.000196494	4.21807e-05	2.9639e-08	3.00123e-08	1.57195e-08	2.2953e-08	1.12603e-08
8.25	8.87022e-05	2.37814e-05	1.96489e-08	1.33969e-08	7.09618e-09	1.01628e-08	5.08319e-09
8.75	5.10512e-05	1.42281e-05	1.2e-08	7.6446e-09	4.08409e-09	5.76205e-09	2.92555e-09
9.5	3.73596e-05	8.60604e-06	6.58321e-09	5.54303e-09	2.98877e-09	4.14836e-09	2.14094e-09
11	1.13427e-05	2.89742e-06	2.37118e-09	1.6651e-09	9.0742e-10	1.23558e-09	6.5001e-10

Table C.3: Data table of the spectrum measured in d+Au 0-20% most central events. The errors reflect the absolute errors. tot. err. reflects the systematic plus statistical error; stat. err. reflects the statistical error; sys. err. reflects the total systematic error; error A reflects the point-to-point systematic error; error B reflects systematic errors that are correlated in p_T but allow the shape of the result to change; error C reflects the normalization error.

p_T	inv. yield	tot. err.	stat. err.	sys. err.	error A	error B	error C
1.25	1.84365	1.10738	0.010812	0.00239358	0.00147492	0.0018131	0.000516223
1.75	0.326715	0.127639	0.00123421	0.000325403	0.000261372	0.00017089	9.14803e-05
2.25	0.102513	0.0290109	0.000271062	0.000103386	8.20101e-05	5.60276e-05	2.87035e-05
2.75	0.0299845	0.00908727	8.50444e-05	3.20201e-05	2.39876e-05	1.94781e-05	8.39566e-06
3.25	0.0107254	0.00343407	3.21948e-05	1.19492e-05	8.58033e-06	7.75519e-06	3.00311e-06
3.75	0.00385913	0.000895012	3.81346e-06	8.09705e-06	3.0873e-06	7.15122e-06	2.21152e-06
4.25	0.00135526	0.000304596	1.51908e-06	2.64012e-06	1.08421e-06	2.2785e-06	7.76648e-07
4.75	0.000577039	0.000128335	7.28248e-07	1.05671e-06	4.61631e-07	8.91169e-07	3.30679e-07
5.25	0.00025794	5.99202e-05	3.96654e-07	4.4912e-07	2.06352e-07	3.70511e-07	1.47816e-07
5.75	0.000143588	3.33912e-05	2.32043e-07	2.40112e-07	1.1487e-07	1.94133e-07	8.22845e-08
6.25	6.97398e-05	1.85083e-05	1.46612e-07	1.12963e-07	5.57918e-08	8.97252e-08	3.99652e-08
6.75	4.62229e-05	1.2721e-05	1.04156e-07	7.30339e-08	3.69783e-08	5.71394e-08	2.64886e-08
7.25	2.58536e-05	7.70742e-06	6.58372e-08	4.00738e-08	2.06829e-08	3.09615e-08	1.48157e-08
7.75	1.20104e-05	2.95943e-06	2.32229e-08	1.83446e-08	9.60832e-09	1.40297e-08	6.8827e-09
8.25	9.45852e-06	2.22554e-06	1.70654e-08	1.42854e-08	7.56682e-09	1.08368e-08	5.42032e-09
8.75	3.88292e-06	1.25647e-06	1.11384e-08	5.81443e-09	3.10633e-09	4.38257e-09	2.22515e-09
9.5	2.39529e-06	6.79728e-07	5.79421e-09	3.55389e-09	1.91623e-09	2.6597e-09	1.37265e-09
11	1.11935e-06	2.94872e-07	2.44845e-09	1.64319e-09	8.95478e-10	1.21932e-09	6.41456e-10

Table C.4: Data table of the spectrum measured in d+Au 20-40% semicentral events. The errors reflect the absolute errors. tot. err. reflects the systematic plus statistical error; stat. err. reflects the statistical error; sys. err. reflects the total systematic error; error A reflects the point-to-point systematic error; error B reflects systematic errors that are correlated in p_T but allow the shape of the result to change; error C reflects the normalization error.

p_T	inv. yield	tot. err.	stat. err.	sys. err.	error A	error B	error C
1.25	0.107607	0.0790788	0.0077835	0.00139704	0.000860853	0.00105824	0.000301299
1.75	0.0137033	0.0087867	0.000868005	0.000136483	0.000109626	7.16757e-05	3.83693e-05
2.25	0.00653853	0.0020148	0.000190383	6.59423e-05	5.23083e-05	3.57359e-05	1.83079e-05
2.75	0.00151989	0.000625226	6.03791e-05	1.62307e-05	1.21591e-05	9.87324e-06	4.25568e-06
3.25	0.000696266	0.000241974	2.29203e-05	7.75712e-06	5.57013e-06	5.03447e-06	1.94954e-06
3.75	0.000217692	5.30508e-05	2.69846e-06	4.56751e-06	1.74153e-06	4.03397e-06	1.24751e-06
4.25	8.53092e-05	1.99166e-05	1.09767e-06	1.66187e-06	6.82474e-07	1.43424e-06	4.88875e-07
4.75	3.57321e-05	8.47171e-06	5.38077e-07	6.54349e-07	2.85857e-07	5.51841e-07	2.04767e-07
5.25	1.45836e-05	4.00893e-06	3.10219e-07	2.53927e-07	1.16669e-07	2.09482e-07	8.35732e-08
5.75	8.11858e-06	2.42145e-06	2.00507e-07	1.35761e-07	6.49487e-08	1.09765e-07	4.65245e-08
6.25	5.71966e-06	1.42353e-06	1.08079e-07	9.26456e-08	4.57573e-08	7.35875e-08	3.27772e-08
6.75	2.43821e-06	9.21434e-07	8.37034e-08	3.85246e-08	1.95057e-08	3.01404e-08	1.39725e-08
7.25	1.26682e-06	3.35683e-07	2.72261e-08	1.96361e-08	1.01346e-08	1.51711e-08	7.25969e-09
7.75	4.9598e-07	1.83525e-07	1.6716e-08	7.57555e-09	3.96784e-09	5.79367e-09	2.84227e-09
8.25	3.86669e-07	1.52865e-07	1.4127e-08	5.83996e-09	3.09336e-09	4.43015e-09	2.21586e-09
8.75	4.33117e-07	1.26659e-07	1.08793e-08	6.48566e-09	3.46493e-09	4.88851e-09	2.48203e-09
9.5	1.6885e-07	5.32417e-08	4.69794e-09	2.50523e-09	1.3508e-09	1.87489e-09	9.67617e-10
11	3.96536e-08	1.52036e-08	1.4045e-09	5.82112e-10	3.17229e-10	4.31951e-10	2.2724e-10

Table C.5: Data table of the spectrum measured in d+Au 40-60% semiperipheral events. The errors reflect the absolute errors. tot. err. reflects the systematic plus statistical error; stat. err. reflects the statistical error; sys. err. reflects the total systematic error; error A reflects the point-to-point systematic error; error B reflects systematic errors that are correlated in p_T but allow the shape of the result to change; error C reflects the normalization error.

p_T	inv. yield	tot. err.	stat. err.	sys. err.	error A	error B	error C
1.25	0.00348995	0.00342517	0.00339507	0.000453093	0.000279196	0.000343212	9.77185e-05
1.75	0.000777771	0.000390015	0.000382245	7.74647e-05	6.22216e-05	4.06816e-05	2.17776e-05
2.25	0.000290426	8.87955e-05	8.38256e-05	2.929e-05	2.32341e-05	1.5873e-05	8.13192e-06
2.75	8.66645e-05	2.82939e-05	2.67375e-05	9.2548e-06	6.93316e-06	5.62976e-06	2.4266e-06
3.25	3.15313e-05	1.10468e-05	1.04733e-05	3.51291e-06	2.5225e-06	2.27992e-06	8.82876e-07
3.75	8.87935e-06	2.25656e-06	1.27326e-06	1.86303e-06	7.10348e-07	1.6454e-06	5.08842e-07
4.25	3.59827e-06	8.6923e-07	5.14015e-07	7.00963e-07	2.87862e-07	6.0495e-07	2.06203e-07
4.75	1.59998e-06	3.95578e-07	2.65771e-07	2.92997e-07	1.27998e-07	2.47097e-07	9.16885e-08
5.25	5.43497e-07	1.80805e-07	1.54063e-07	9.46326e-08	4.34797e-08	7.80691e-08	3.11457e-08
5.75	3.76966e-07	1.05405e-07	8.44773e-08	6.30375e-08	3.01573e-08	5.09666e-08	2.16025e-08
6.25	2.52057e-07	4.94033e-08	2.78171e-08	4.08276e-08	2.01646e-08	3.2429e-08	1.44445e-08
6.75	1.22674e-07	2.73258e-08	1.92613e-08	1.9383e-08	9.81394e-09	1.51646e-08	7.02999e-09
7.25	5.24508e-08	1.57209e-08	1.34555e-08	8.12999e-09	4.19606e-09	6.28134e-09	3.00575e-09
7.75	4.0941e-08	1.11914e-08	9.28143e-09	6.25328e-09	3.27528e-09	4.78242e-09	2.34617e-09
8.25	1.7928e-08	8.47401e-09	8.02976e-09	2.70771e-09	1.43424e-09	2.05405e-09	1.02738e-09
8.75	4.86946e-09	6.22577e-09	6.18292e-09	7.29171e-10	3.89557e-10	5.49606e-10	2.7905e-10
9.5	6.43159e-09	2.79294e-09	2.62486e-09	9.54254e-10	5.14527e-10	7.14156e-10	3.6857e-10
11	1.3009e-10	1.85436e-09	1.85426e-09	1.90971e-11	1.04072e-11	1.41709e-11	7.45498e-12

Table C.6: Data table of the spectrum measured in d+Au 60-88% peripheral events. The errors reflect the absolute errors. tot. err. reflects the systematic plus statistical error; stat. err. reflects the statistical error; sys. err. reflects the total systematic error; error A reflects the point-to-point systematic error; error B reflects systematic errors that are correlated in p_T but allow the shape of the result to change; error C reflects the normalization error.

p_T	R_{dA}	tot. err.	tot. err. A	error B	error C
1.75	1.06619	0.557127	0.549293	0.0373168	0.0852954
2.25	1.78536	0.594115	0.573295	0.0624878	0.142829
2.75	1.15302	0.404245	0.391506	0.0403558	0.0922418
3.25	0.843394	0.320033	0.311444	0.0295188	0.0674715
3.75	1.12681	0.193921	0.0992608	0.140095	0.0901445
4.25	1.06125	0.179095	0.105579	0.117134	0.0848997
4.75	1.11981	0.1859	0.119342	0.110865	0.0895845
5.25	0.942403	0.179205	0.138835	0.0845891	0.0753923
5.75	1.00012	0.238699	0.209303	0.0822667	0.0800098
6.25	1.12363	0.250713	0.21783	0.085596	0.0898908
6.75	0.996127	0.231609	0.205557	0.0709817	0.0796901
7.25	0.73016	0.227801	0.214635	0.0491236	0.0584128
7.75	1.18934	0.355021	0.33344	0.0761878	0.0951475
8.25	1.25095	0.406166	0.386064	0.0768753	0.100076
8.75	0.985461	0.340084	0.32561	0.0584804	0.0788369

Table C.7: Data table of R_{dA} for η minimum bias. The errors reflect the absolute errors. Tot. err. reflects both the statistical and the systematic errors. Tot. err. A reflects the quadratic sum of the statistical and the point-to-point systematic error; error B reflects systematic errors that are correlated in p_T but allow the shape of the result to change; error C reflects the normalization error.

p_T	R_{dA}	tot. err.	tot. err. A	error B	error C
1.75	1.1045	0.546401	0.537822	0.0386575	0.08836
2.25	1.42378	0.531885	0.51715	0.0498321	0.113902
2.75	1.02911	0.388691	0.37816	0.0360188	0.0823287
3.25	0.662183	0.316077	0.310743	0.0231764	0.0529747
3.75	1.10951	0.18865	0.0931761	0.137945	0.088761
4.25	1.08562	0.179398	0.101405	0.119824	0.0868497
4.75	1.13563	0.183875	0.113645	0.112431	0.0908504
5.25	1.06159	0.186029	0.135331	0.0952867	0.0849268
5.75	1.04317	0.237752	0.205423	0.0858073	0.0834533
6.25	1.05626	0.240468	0.210262	0.0804639	0.0845011
6.75	0.960946	0.223569	0.198455	0.0684749	0.0768757
7.25	0.881855	0.233068	0.214065	0.0593294	0.0705484
7.75	1.2531	0.32724	0.300986	0.0802718	0.100248
8.25	0.992926	0.376065	0.36248	0.0610188	0.0794341
8.75	1.0061	0.340375	0.325288	0.0597051	0.0804878

Table C.8: Data table of R_{dA} for η 0-20 % most central events. The errors reflect the absolute errors. Tot. err. reflects both the statistical and the systematic errors. Tot. err. A reflects the quadratic sum of the statistical and the point-to-point systematic error; error B reflects systematic errors that are correlated in p_T but allow the shape of the result to change; error C reflects the normalization error.

p_T	R_{dA}	tot. err.	tot. err. A	error B	error C
1.75	0.879227	0.543321	0.537869	0.0307729	0.0703381
2.25	1.47882	0.534611	0.518781	0.0517588	0.118306
2.75	0.909104	0.386599	0.378361	0.0318186	0.0727283
3.25	0.768798	0.318224	0.311063	0.0269079	0.0615038
3.75	1.07248	0.184114	0.0935783	0.133341	0.0857987
4.25	0.943916	0.163849	0.101439	0.104184	0.0755133
4.75	1.01436	0.172144	0.113856	0.100425	0.0811484
5.25	0.955058	0.177711	0.135627	0.0857249	0.0764046
5.75	1.04794	0.238464	0.205929	0.0861996	0.0838348
6.25	1.02585	0.239394	0.210873	0.0781467	0.0820677
6.75	1.13811	0.234415	0.200208	0.0810993	0.091049
7.25	1.07332	0.243006	0.215556	0.072211	0.085866
7.75	1.07374	0.320653	0.301179	0.0687825	0.0858994
8.25	1.48427	0.394272	0.364734	0.0912136	0.118742
8.75	1.07275	0.343498	0.326455	0.0636607	0.0858203

Table C.9: Data table of R_{dA} for η 20-40 % semicentral events. The errors reflect the absolute errors. Tot. err. reflects both the statistical and the systematic errors. Tot. err. A reflects the quadratic sum of the statistical and the point-to-point systematic error; error B reflects systematic errors that are correlated in p_T but allow the shape of the result to change; error C reflects the normalization error.

p_T	R_{dA}	tot. err.	tot. err. A	error B	error C
1.75	0.571862	0.540287	0.537975	0.0200152	0.045749
2.25	1.4627	0.539649	0.524317	0.0511944	0.117016
2.75	0.714599	0.383952	0.378847	0.025011	0.0571679
3.25	0.773941	0.319241	0.312005	0.0270879	0.0619153
3.75	0.938162	0.167824	0.0944826	0.116641	0.075053
4.25	0.921386	0.162203	0.102637	0.101697	0.0737109
4.75	0.974044	0.169439	0.11549	0.0964338	0.0779235
5.25	0.837357	0.169848	0.136791	0.0751603	0.0669886
5.75	0.918825	0.232791	0.207548	0.0755794	0.073506
6.25	1.30469	0.259905	0.216283	0.0993882	0.104375
6.75	0.930965	0.226126	0.202941	0.0663385	0.0744772
7.25	0.815568	0.231004	0.214698	0.0548697	0.0652455
7.75	0.687609	0.309313	0.301178	0.0440473	0.0550087
8.25	0.940946	0.377475	0.365345	0.0578244	0.0752757
8.75	1.85559	0.397715	0.352157	0.110117	0.148447

Table C.10: Data table of R_{dA} for η 40-60 % semiperipheral events. The errors reflect the absolute errors. Tot. err. reflects both the statistical and the systematic errors. Tot. err. A reflects the quadratic sum of the statistical and the point-to-point systematic error; error B reflects systematic errors that are correlated in p_T but allow the shape of the result to change; error C reflects the normalization error.

p_T	R_{dA}	tot. err.	tot. err. A	error B	error C
1.75	0.699869	0.545951	0.54252	0.0244954	0.0559895
2.25	1.4009	0.561103	0.547606	0.0490316	0.112072
2.75	0.8786	0.393025	0.385464	0.030751	0.070288
3.25	0.755743	0.323354	0.316549	0.026451	0.0604594
3.75	0.825119	0.157002	0.0988361	0.102586	0.0660095
4.25	0.837989	0.156561	0.107062	0.092492	0.0670391
4.75	0.940441	0.172381	0.12404	0.093107	0.0752353
5.25	0.672886	0.162587	0.141028	0.0603975	0.0538309
5.75	0.919928	0.239127	0.214569	0.0756702	0.0735943
6.25	1.23975	0.25931	0.220195	0.0944416	0.0991802
6.75	1.00998	0.232672	0.205981	0.0719692	0.0807988
7.25	0.728106	0.231016	0.218119	0.0489855	0.0582485
7.75	1.22387	0.344659	0.321025	0.0783994	0.0979094
8.25	0.940709	0.394998	0.38343	0.0578098	0.0752567
8.75	0.449838	0.33757	0.334584	0.0266948	0.035987

Table C.11: Data table of R_{dA} for η 60-88 % most peripheral events. The errors reflect the absolute errors. Tot. err. reflects both the statistical and the systematic errors. Tot. err. A reflects the quadratic sum of the statistical and the point-to-point systematic error; error B reflects systematic errors that are correlated in p_T but allow the shape of the result to change; error C reflects the normalization error.

p_T	R_{dA}	tot. err.	tot. err. A	error B	error C
1.25	0.0952543	0.164099	0.163566	0.0108007	0.00762034
1.75	0.267874	0.147353	0.143957	0.0230208	0.0214299
2.25	0.241728	0.127997	0.124735	0.0212253	0.0193382
2.75	0.417728	0.166706	0.158447	0.0396052	0.0334182
3.25	0.578988	0.197348	0.182775	0.058261	0.0463191
3.75	0.436392	0.106847	0.0511785	0.0870526	0.0349113
4.25	0.49326	0.112445	0.0510484	0.0920908	0.0394608
4.75	0.488587	0.110997	0.0587649	0.08567	0.039087
5.25	0.495197	0.116228	0.0710689	0.0829992	0.0396157
5.75	0.49623	0.137796	0.104109	0.0810745	0.0396984
6.25	0.546735	0.154553	0.119708	0.0874267	0.0437388
6.75	0.542422	0.149917	0.115109	0.0856854	0.0433938
7.25	0.658801	0.195261	0.157485	0.102703	0.0527041
7.75	0.619331	0.23343	0.206863	0.0961391	0.0495465
8.25	0.396352	0.170524	0.155457	0.062499	0.0317081
8.75	0.433374	0.181495	0.164625	0.0680962	0.0346699
9.5	0.561388	0.225465	0.202488	0.0884088	0.044911

Table C.12: Data table of the ratio of η and π^0 for min. bias p+p events. The errors reflect the absolute errors. Tot. err. reflects both the statistical and the systematic errors. Tot. err. A reflects the quadratic sum of the statistical and the point-to-point systematic error; error B reflects systematic errors that are correlated in p_T but allow the shape of the result to change; error C reflects the normalization error.

p_T	R_{dA}	tot. err.	tot. err. A	error B
1.25	0.257888	0.0848246	0.0813259	0.0241104
1.75	0.308016	0.0834153	0.0822324	0.0139977
2.25	0.424765	0.121319	0.120902	0.0100517
2.75	0.465527	0.143655	0.143492	0.00684166
3.25	0.451947	0.0610156	0.0607779	0.00538049
3.75	0.439544	0.0565707	0.0563228	0.00529065
4.25	0.4721	0.0753924	0.0751222	0.00637652
4.75	0.457269	0.0894427	0.0891597	0.00710991
5.25	0.433331	0.0621057	0.0616251	0.00771081
5.75	0.500967	0.0917317	0.0911791	0.0100534
6.25	0.553873	0.124195	0.12358	0.0123442
6.75	0.555848	0.150676	0.150063	0.0135696
7.25	0.426936	0.086289	0.0855482	0.0112823
7.75	0.558553	0.276781	0.276328	0.0158183
8.25	0.662492	0.330061	0.329458	0.0199348

Table C.13: Data table of the ratio of η and π^0 for min. bias d+Au events. The errors reflect the absolute errors. Tot. err. reflects both the statistical and the systematic errors. Tot. err. A reflects the quadratic sum of the statistical and the point-to-point systematic error; error B reflects systematic errors that are correlated in p_T but allow the shape of the result to change.

p_T	R_{dA}	tot. err.	tot. err. A	error B
1.25	0.141697	0.18049	0.180004	0.0132475
1.75	0.311249	0.120889	0.120058	0.0141447
2.25	0.316067	0.110094	0.10984	0.00747947
2.75	0.394178	0.124804	0.12467	0.00579307
3.25	0.335173	0.13599	0.135932	0.00399028
3.75	0.449803	0.0782017	0.0780141	0.00541413
4.25	0.455115	0.0781388	0.0778967	0.00614711
4.75	0.458137	0.082722	0.0824147	0.00712341
5.25	0.487126	0.0947067	0.0943092	0.00866807
5.75	0.50871	0.109855	0.10938	0.0102088
6.25	0.519175	0.134785	0.134288	0.0115709
6.75	0.542306	0.154143	0.153573	0.013239
7.25	0.549227	0.197374	0.19684	0.014514
7.75	0.651226	0.16266	0.161611	0.0184428
8.25	0.435791	0.140221	0.139606	0.0131132
8.75	0.445311	0.156312	0.155672	0.0141323
9.5	0.840119	0.253557	0.251946	0.0285369

Table C.14: Data table of the ratio of η and π^0 for 0-20 % most central d+Au events. The errors reflect the absolute errors. Tot. err. reflects both the statistical and the systematic errors. Tot. err. A reflects the quadratic sum of the statistical and the point-to-point systematic error; error B reflects systematic errors that are correlated in p_T but allow the shape of the result to change.

p_T	R_{dA}	tot. err.	tot. err. A	error B
1.25	0.288594	0.197637	0.195787	0.0269812
1.75	0.264626	0.119717	0.119111	0.0120259
2.25	0.355838	0.118971	0.118672	0.00842063
2.75	0.368526	0.129274	0.129161	0.00541608
3.25	0.433875	0.159993	0.15991	0.00516535
3.75	0.468188	0.0849634	0.0847763	0.00563543
4.25	0.417131	0.0801448	0.0799465	0.00563407
4.75	0.406864	0.0831185	0.0828775	0.00632618
5.25	0.4363	0.100157	0.0998554	0.00776365
5.75	0.51482	0.122896	0.122461	0.0103315
6.25	0.480085	0.137436	0.137019	0.0106997
6.75	0.604514	0.184767	0.184177	0.0147577
7.25	0.608309	0.206718	0.206092	0.0160753
7.75	0.530385	0.158494	0.15778	0.0150206
8.25	0.639366	0.194654	0.1937	0.0192389
8.75	0.483948	0.205802	0.205228	0.0153585
9.5	0.662681	0.245135	0.2441	0.0225098

Table C.15: Data table of the ratio of η and π^0 for 20-40 % semicentral d+Au events. The errors reflect the absolute errors. Tot. err. reflects both the statistical and the systematic errors. Tot. err. A reflects the quadratic sum of the statistical and the point-to-point systematic error; error B reflects systematic errors that are correlated in p_T but allow the shape of the result to change.

p_T	R_{dA}	tot. err.	tot. err. A	error B
1.25	0.264609	0.215188	0.213761	0.0247388
1.75	0.177789	0.125083	0.124822	0.0080796
2.25	0.364795	0.131574	0.131291	0.00863261
2.75	0.315959	0.146176	0.146102	0.00464352
3.25	0.449929	0.179374	0.179294	0.00535646
3.75	0.416364	0.0844053	0.0842564	0.00501164
4.25	0.429411	0.0888111	0.0886215	0.00579993
4.75	0.419464	0.0949823	0.0947581	0.0065221
5.25	0.407585	0.116278	0.116051	0.00725268
5.75	0.479617	0.154302	0.154001	0.009625
6.25	0.632936	0.171326	0.170744	0.0141063
6.75	0.488886	0.207405	0.207061	0.0119349
7.25	0.494299	0.15492	0.154369	0.0130625
7.75	0.349485	0.157875	0.157564	0.00989749
8.25	0.429251	0.214474	0.214085	0.0129164
8.75	1.11347	0.461506	0.460151	0.035337
9.5	1.6885e-08	4.92181e-09	4.88828e-09	5.73546e-10

Table C.16: Data table of the ratio of η and π^0 for 40-60 % semiperipheral d+Au events. The errors reflect the absolute errors. Tot. err. reflects both the statistical and the systematic errors. Tot. err. A reflects the quadratic sum of the statistical and the point-to-point systematic error; error B reflects systematic errors that are correlated in p_T but allow the shape of the result to change.

p_T	R_{dA}	tot. err.	tot. err. A	error B
1.25	0.19782	0.210503	0.209689	0.0184946
1.75	0.236698	0.132896	0.132459	0.0107567
2.25	0.389832	0.139327	0.139022	0.00922508
2.75	0.434278	0.164814	0.164691	0.0063824
3.25	0.512805	0.208233	0.208144	0.00610501
3.75	0.443491	0.0977722	0.0976264	0.00533815
4.25	0.46201	0.102011	0.10182	0.00624024
4.75	0.479362	0.11603	0.11579	0.00745343
5.25	0.371769	0.132111	0.131946	0.00661536
5.75	0.520545	0.158445	0.1581	0.0104463
6.25	0.696911	0.145806	0.144976	0.0155321
6.75	0.617113	0.159969	0.159258	0.0150653
7.25	0.486366	0.179047	0.178585	0.0128528
7.75	0.601333	0.21186	0.211175	0.0170299
8.25	0.437752	0.255862	0.255523	0.0131722
8.75	0.251238	0.364487	0.364399	0.00797327
9.5	0.598201	0.340208	0.339601	0.0203195

Table C.17: Data table of the ratio of η and π^0 for 60-88 % most peripheral d+Au events. The errors reflect the absolute errors. Tot. err. reflects both the statistical and the systematic errors. Tot. err. A reflects the quadratic sum of the statistical and the point-to-point systematic error; error B reflects systematic errors that are correlated in p_T but allow the shape of the result to change.

Bibliography

[Ack03] K.H. Ackermann et. al., Nucl. Instrum. Meth. **A 499** (2003) 624.

[Ada03] M. Adamczyk et. al., Nucl. Instrum. Meth. **A 499** (2003) 437.

[Adc03a] K. Adcox et. al., Nucl. Instrum. Meth. **A 499** (2003) 469.

[Adc03b] K. Adcox et. al., Nucl. Instrum. Meth. **A 499** (2003) 489.

[Adl03a] S.S. Adler et. al., Phys. Rev. Lett. **91** (2003) 072301.

[Adl03b] S.S. Adler et. al., Phys. Rev. Lett. **91** (2003) 072303.

[Adl03c] S.S. Adler et. al., Phys. Rev. Lett. **91** (2003) 241803.

[Adl03d] S.S. Adler et. al., Phys. Rev. Lett. **91** (2003) 172301.

[Aiz03] M. Aizawa et. al., Nucl. Instrum. Meth. **A 499** (2003) 508.

[Aki03] H. Akikawa et. al., Nucl. Instrum. Meth. **A 499** (2003) 537.

[All03] M. Allen et. al., Nucl. Instrum. Meth. **A 499** (2003) 549.

[Ant79] D. Antreasyan et al., Phys. Rev. **D 19** (1979) 764.

[Aph03a] L. Aphecetche et. al., Nucl. Instrum. Meth. **A 499** (2003) 521.

[Aph03b] L. Aphecetche et al., *Neutral Pion Spectra measured with the EmCal in* $\sqrt{s_{NN}}$ *= 200 GeV d+Au-Collisions*, PHENIX internal analysis note AN203, BNL, Upton, New York, 2003.

[Aro03] S.H. Aronson et. al., Nucl. Instrum. Meth. **A 499** (2003) 480.

[Awe01] T.C. Awes et. al., *Neutral Pion Spectra from the Leadglass Calorimeter*, PHENIX internal analysis note AN069, BNL, Upton, New York, 2001.

[Bac03] B.B. Back et. al., Nucl. Instrum. Meth **A 499** (2003) 603.

[Bai95] R. Baier et. al., Phys. Lett. **B 345** (1995) 277.

[Bai97a] R. Baier et. al., Nucl. Phys. **B 483** (1997) 291.

[Bai97b] R. Baier et. al., Nucl. Phys. **B 484** (1997) 265.

[Bai00] R. Baier, D. Schiff and B.G. Zakharov, Ann. Rev. Nucl. Part. Sci. **50** (2000) 37.

[Bat02] S. Bathe, *Impulsfluktuationen und Produktion neutraler Pionen in ultrarelativistischen Schwerionenreaktionen*, Dissertation, Institut für Kernphysik, Münster, 2002.

[Bat03] S. Bathe et. al., *Centrality Dependence of Neutral Pion Spectra measured with the EMCal in* $\sqrt{s_{NN}}$ *= 200 GeV d+Au-Collisions*, PHENIX internal analysis note AN234, BNL, Upton, New York, 2003.

[Baz02] S. Bazilevsky et. al., *Absolute cross section for* π^0 *production in proton-proton collisions at* $\sqrt{s}$ *= 200 GeV*, PHENIX internal analysis note AN176, BNL, Upton, New York, 2002.

[Bjo83] J.D. Bjørken, Phys. Rev. D **27** (1983) 140.

[BNL03] BNL press release, http://www.bnl.gov/bnlweb/pubaf/pr/2003/bnlpr061103.htm BNL, Upton, 2003.

[Bra01] P. Braun-Munzinger and J. Stachel, Preprint nucl-th/0112051.

[Bus02] H. Büsching, *Azimuthale Photonen-Korrelationen in ultrarelativistischen p+A-, Pb+Pb- und Au+Au-Reaktionen*, Dissertation, Institut für Kernphysik, Münster, 2002.

[Cle98] J. Cleymans and K. Redlich, Phys Rev. Lett. **81** (1998) 5284.

[dEn03] D. d'Enterria, J. Frantz, S.Mioduszewski, *High p_T η Measurement in the PbSc Calorimeter in Au+Au collisions at $\sqrt{s_{NN}}$ = 200 GeV*, PHENIX internal analysis note AN235, BNL, Upton, New York, 2003.

[dEn04] D. d'Enterria, *Nucleon-nucleon reference p_T distribution for inclusive π^0 production in Au+Au collisions at $\sqrt{s_{NN}}$ = 62.4 GeV*, PHENIX internal analysis note AN291, BNL, Upton, New York, 2004.

[Dre03] A. Drees et. al., *Centrality determination and pT centrality dependency in d-Au collisions.*, PHENIX internal analysis note AN210, BNL, Upton, New York, 2003.

[Gyu90] M. Gyulassy and M. Plumer, Phys. Lett. **B 243** (1990) 432.

[Hag83] R. Hagedorn, *Multiplicities, p_T distributions and the expected Hadron to Quark-Gluon Phase Transition*, CERN-TH. 3684, 1983.

[Hag02] K. Hagiwara et. al., Phys. Rev. **D 66** (2002) 010001.

[Hah03] H. Hahn et. al., Nucl. Instrum. Meth. **A 499** (2003) 245.

[Har96] J.W. Harris and Berndt Müller, Ann. Rev. Nucl. Part. Sci. **46** (1996) 71.

[Ian03] E. Iancu and R. Venugopalan, Preprint hep-ph/0303204.

[Kle03] C. Klein-Bösing et. al., *Neutral Pion Spectra measured with the PbGl in $\sqrt{s_{NN}}$ = 200 GeV AuAu-Collisions*, PHENIX internal analysis note AN167, BNL, Upton, New York, 2003.

[Lan53] L.D. Landau and I. Pomeranchuk, Dokl. Akad. Nauk Ser. Fiz. **92** (1953) 735.

[Mer00] M. Merschmeyer, *Das Bleiglaskalorimeter in der Simulationsumgebung des PHENIX-Experiments*, Diplomarbeit, Institut für Kernphysik, Münster, 2000.

[Mig56] A.B. Migdal, Phys. Rev. **103** (1956) 1811.

[Owe78] J.F. Owens *et al.*, Phys. Rev. **D 18** (1978) 1501.

[Per90] D.H. Perkins, *Hochenergiephysik*, Addison-Wesley, 1990.

[Pil00] G. Piller and W. Weise, Phys. Rept. **330** (2000) 1.

[Rey99] K. Reygers, *Teilchenproduktion in ultrarelativistischen p+Pb und Pb+Pb-Reaktionen*, Dissertation, Institut für Kernphysik, Münster, 1999.

[Rey03] K. Reygers et. al., *Measurement of Neutral Pions in $\sqrt{s}$=200 GeV p+p-Collisions with the PbGl Calorimeter*, PHENIX internal analysis note AN175, BNL, Upton, New York, 2003.

[Sjo94] T. Sjøstrand, Comput. Phys. Commun. **82** (1994) 74.

[Wan01] E. Wang and X.N. Wang, Phys. Rev. **C 64** (2001) 034901.

[Won94] C.Y. Wong, *Introduction to High-Energy Heavy-Ion Collisions*, World Scientific, 1994.

Acknowledgment

A lot of people gave contributions to this diploma thesis and helped me writing it. I would like to thank all of them here:

I thank Prof. Dr. Johannes P. Wessels for providing the opportunity of writing this thesis in his working group at the Institut für Kernphysik in Münster. The atmosphere in the group was very nice. I was given the chance for a very interesting visit at BNL and the participation in the DPG spring meeting in Cologne.

I would like to acknowledge Dr. Klaus Reygers who supervised this thesis for his guidance and support and the constant willingness to discuss different questions and problems.

I thank Dr. Stefan Bathe and Dr. Henner Büsching for their support during my visit at BNL as well as for answering many of my questions and providing me with necessary information.

I acknowledge Dr. Damian Bucher for accompanying me to BNL and for discussing several questions as well.

I also thank the other people in our two office rooms in the second floor: Christian Klein-Bösing for providing assistance with analysis and software questions; Oliver Zaudtke and Alexander Wilk for answering my questions. I like to acknowledge these three guys as well as Melanie Hoppe and Jan Auffenberg for the good atmosphere in the office.

I like to thank the "η group" of PHENIX for their contributions to this work, their support and their suggestions. By name, they are Dr. David d'Enterria, Dr. Henner Büsching, Justin Frantz, Hiroyoshi Hiejima, Maike Kaufman, Dr. Saskia Mioduszewski and Dr. Klaus Reygers.

I thank Prof. Dr. Rainer Santo for his suggestions. I also like to thank the PHENIX collaboration which made this work possible.

I thank the other members of the working groups of Prof. Wessels and Prof. Santo, Heinz-Hermann Adam, Christoph Baumann, Dr. Richard Glasow, Holger Gottschlag, Norbert Heine, Dr. Alfons Khoukaz, Thorsten Korfsmeyer, Dr. Norbert Lang, Ricarda Menke, Timo Mersmann, Tobias Rausmann, Alexander Täschner, Wolfgang Verhoeven for their support and the pleasant teamwork. I also thank Michaela Ohagen and Uta Mayer for their administrative support.

I like to acknowledge Dr. Damian Bucher, Dr. Klaus Reygers and Maike Rocker for the critical review and their helpful annotations.

Last but not least I thank my parents and my family for supporting me during my study and of course during my whole life, and I thank my friends for being there.

Hiermit bestätige ich, dass ich diese Arbeit selbstständig verfasst und keine anderen als die angegebenen Quellen und Hilfsmittel verwendet habe.

Münster, 23. August 2004

Baldo Sahlmüller